Acta Biomaterialia 86 (2019) 77–95

Contents lists available at ScienceDirect

Acta Biomaterialia

journal homepage: www.elsevier.com/locate/actabiomat

Full length article

Tensile behavior and structural characterization of pig dermis

Andrei Pissarenko [a], Wen Yang [a,b,*], Haocheng Quan [a], Katherine A. Brown [c,d], Alun Williams [e], William G. Proud [f], Marc A. Meyers [a,*]

[a] University of California, San Diego, CA, USA
[b] Lawrence Berkeley National Laboratory, USA
[c] Cavendish Laboratory, University of Cambridge, Cambridge, UK
[d] Department of Chemistry, The University of Texas at Austin, Austin, Texas, USA
[e] Department of Veterinary Medicine, University of Cambridge, Cambridge, UK
[f] Institute of Shock Physics, Imperial College London, London, UK

ARTICLE INFO

Article history:
Received 2 August 2018
Received in revised form 10 January 2019
Accepted 14 January 2019
Available online 16 January 2019

Keywords:
Skin
Collagen
Stress relaxation
TEM
Pig
Mechanical properties

ABSTRACT

Skin, the outermost layer of the body, fulfills a broad range of functions, protecting internal organs from damage and infection, while regulating the body's temperature and water content via the exchange of heat and fluids. It must be able to withstand and recover from extensive deformation and damage that can occur during growth, movement, and potential injuries. A detailed investigation of the evolution of the collagen architecture of the dermis as a function of deformation is conducted, which reveals new aspects that help us to understand the mechanical response of skin. Juvenile pig is used as a model material because of its similarity to human skin. The dermis is found to have a tridimensional woven structure of collagen fibers, which evolves with deformation. After failure, we observe that the fibers have straightened and aligned in the direction of tension. The effects of strain-rate change, cyclic loading, stress relaxation, and orientation are quantitatively established. Digital image correlation techniques are implemented to quantify skin's anisotropy; measurements of the Poisson ratio are reported. This is coupled with transmission electron microscopy which enables obtaining quantitative strain parameters evaluated through the orientation and curvature of the collagen fibers and their changes, for the first time in all three dimensions of the tissue. A model experiment using braided human hair in tension exhibits a similar J-curve response to skin, and we propose that this fiber configuration is at least partially responsible for the monotonic increase of the tangent modulus of skin with strain. The obtained results are intended to serve as a basis for structurally-based models of skin.

Statement of Significance

Our study reveals a new aspect of the dermis: it is comprised of a tridimensional woven structure of collagen fibers, which evolves with deformation. This is enabled by primarily two techniques, transmission electron microscopy on three perpendicular planes and confocal images with second harmonic generation fluorescence of collagen, captured at different intervals of depth. After failure, the fibers have straightened and aligned in the direction of tension. Digital image correlation techniques are implemented to quantify skin's anisotropy; measurements of the Poisson ratio are reported. A model experiment using braided human hair in tension exhibits a similar J-curve response to skin, and we propose that this fiber configuration is at least partially responsible for the monotonic increase of the tangent modulus of skin with strain.

1. Introduction

The mechanical performance of skin is essential in ensuring that it can maintain its integrity throughout life, and therefore satisfy its primary functions of protection, sensing regulation via fluids, and heat exchange. It is the largest organ of the body of mammals,

* Corresponding authors at: University of California, San Diego, CA, USA.
E-mail addresses: wyang8207@gmail.com (W. Yang), mameyers@eng.ucsd.edu (M.A. Meyers).

https://doi.org/10.1016/j.actbio.2019.01.023
1742-7061/

and its structure is a composite of three distinct layers that fulfill different functions, e.g., [1]: the epidermis (∼50 to 150 μm for humans [2,3]), is a hard keratinized layer at the surface of the tissue, lying on top of the dermis (∼0.15 to 4 mm thickness [4,5]), the load-bearing component of skin formed by a complex arrangement of collagen (∼70% of the dry weight of skin) and elastin (∼2 to 4% of the dry weight of skin) fibers [4–6]; the hypodermis is the inner layer, mostly consisting of fat lobules that provide shock absorption and minimize friction with the internal organs of the body [4,5]. Thus, tensile properties are mostly provided by the dermis, and understanding the processes at play during deformation can be useful in a wide range of applications such as surgery, biomedical engineering, dermal armor, wearable devices, and biomimetics.

A significant amount of research on the mechanical behavior of the skin has shown that it is an anisotropic, non-linear elastic material that exhibits viscoelasticity and loading history dependence [4,6–9]. These properties can be attributed to the structure of the dermis, and the arrangement of its constitutive elements as well of their respective mechanical properties. Collagen fibrils, ∼50 to 500 nm in diameter, are characterized by a d-period of 67 nm, due to the staggered arrangement of tropocollagen molecules, which have a length of ∼300 nm and a diameter of ∼1.5 nm. Bundled fibrils form collagen fibers, with diameters ranging 2–7 μm in skin [10,11]. In the dermis, these collagen fibers are organized into a complex three-dimensional network, an arrangement that is not fully understood yet. Depending on the location on the body, collagen fibers follow preferred orientations in planes parallel to the outer surface, an alignment that can be related to pre-existing lines of tension in skin, i.e. the Langer lines [11–15], and therefore the material's anisotropy. Jor et al. [16] measured angular distributions of collagen fibers from confocal imaging of cross-sections of pig skin, and reported that the fibers tend to be oriented at ±45° with the normal direction to the outer surface, showing an important out-of-plane component in the undeformed configuration as well. Collagen fibers are initially crimped [11,17,18], and progressively straighten under tensile loading, explaining the non-linear elasticity of the tissue. At higher levels of strain, straight fibers slide past each other, and eventually delaminate, until failure occurs [19]. During this process, interfibrillar shearing is an additional factor of influence on non-linearity, but also on viscoelasticity and energy dissipation in skin. The surrounding ground substance (comprised of proteoglycans) also highly contributes to skin's viscoelasticity. The contribution of elastin in the overall mechanical behavior of skin is often discussed [20–23], mainly due to its low weight percentage and relatively little influence at high strains, and some researchers claim that it plays an important role in the recoil of skin at low stresses [17,24–26]. Thus, it is important to understand and measure changes in the structural configuration of the constitutive elements of skin during the deformation process in order to associate the macroscopic behavior with microscale phenomena.

Various experimental techniques have been applied to characterize skin's mechanical properties, involving torsion [27–30], suction [31–35], indentation [36–39], uniaxial [40–45], biaxial [46,47], and multiaxial [48] tests, which can be conducted either *in vivo* or *ex vivo*. For a full characterization, *ex vivo* testing is preferred, so that the material can be tested until failure, or with irreversible damage. Under such conditions, uniaxial tensile tests are generally favored for their ease of implementation and standardized methods, and consequently a broad range of reported data in the literature enable comparison. Although biaxial testing is more suitable to assess tissue anisotropy, the method also comes with additional complications and restrictions that can compromise the accuracy, as well as the completeness of experimental results (sample gripping and slipping, inability to reach failure). Anisotropy can be partially quantified by testing different tissue orientations. The typical J-shaped stress-strain curve of skin can then be used to extract information on failure strain, failure stress, tangent moduli, deformation energy, and anisotropy [40,41,44]. Experimental setups are sometimes coupled with imaging techniques, such as Optical Coherence Tomography [49,50], or Digital Image Correlation (DIC) [33,40], mainly for increased accuracy of the measured deformation, and quantification of sample anisotropy via the measurement of lateral strains. Nonetheless, the obtained data are seldom used to evaluate the Poisson ratio, which can yield additional insight into the deformation process within the material. Lees et al. [51] reported values of the Poisson ratio for cow teat skin ranging from −0.8 to 2.0, with variations mainly caused by differences in sample geometry, loading conditions, and strain state, which is also encountered in knitted fabrics. Such large values are far from classic incompressible materials, such as rubber and silicone (0.4–0.5), to which skin is often compared.

Monitoring microstructural changes during the process of deformation is a more challenging task, and has been conducted *ex situ* using Scanning Electron Microscopy (SEM) [19,21], and *in situ* with Small Angle X-Ray Scattering (SAXS) [19] or Small Angle Light Scattering (SALS) [52], and Second Harmonic Generation (SHG) microscopy [53]. The straightening and realignment process of collagen fibers in the direction of applied tension is evident, and sliding and delamination are also observed at high strains. However, it remains unclear whether a certain degree of entanglement between fibers exists, which would generate additional shearing constraints, irreversible damage, and out-of-plane effects. It is also important to note that such observations are mostly done parallel to the surface of the skin, implying that processes occurring out-of-plane are rarely reported.

The work presented in this study aims to expand our understanding on the mechanical behavior of skin, from uniaxial tensile tests conducted on freshly excised porcine skin. The same testing method is applied for all loading cases and samples to maintain consistency of results. We connect the change in collagen configuration, obtained by TEM, to the evolution of damage. This is conducted on three perpendicular planes for the initial, undeformed, configuration as well as after failure. Particular attention is given to the processes of rearrangement occurring within the structure, both at a macroscopic level with assessments of irreversibility of the deformation and changes in the Poisson ratio, and at the microscale via a quantitative analysis of the realignment of collagen in the dermis. Pig skin was chosen for this study because of its similarity with human skin and because it is relatively easy to obtain fresh samples.

2. Methods and materials

2.1. Sample preparation

Porcine skin from two sources was used in the present investigation. The Veterinary School at the University of Cambridge (UK) provided two nine-week old pigs whose skin was excised shortly after being sacrificed. The excess fat on the hypodermis was cut down. The orientations of the obtained specimens are shown in Fig. 1a. Both transverse (perpendicular to the direction of the spine) and longitudinal (parallel to the direction of the spine) hourglass-shaped specimens were removed using a cutting die, following the geometry described by the ASTM D412 Type B standard [54] for testing of rubbers and elastomers (Fig. 1b). To account for sample shrinkage or expansion due to pre-existing tension *in vivo*, dimensions were also measured after excision. The skin was subsequently wrapped in cellophane and stored in a cold room at 4 °C to preserve freshness. Samples were left at room temperature a few

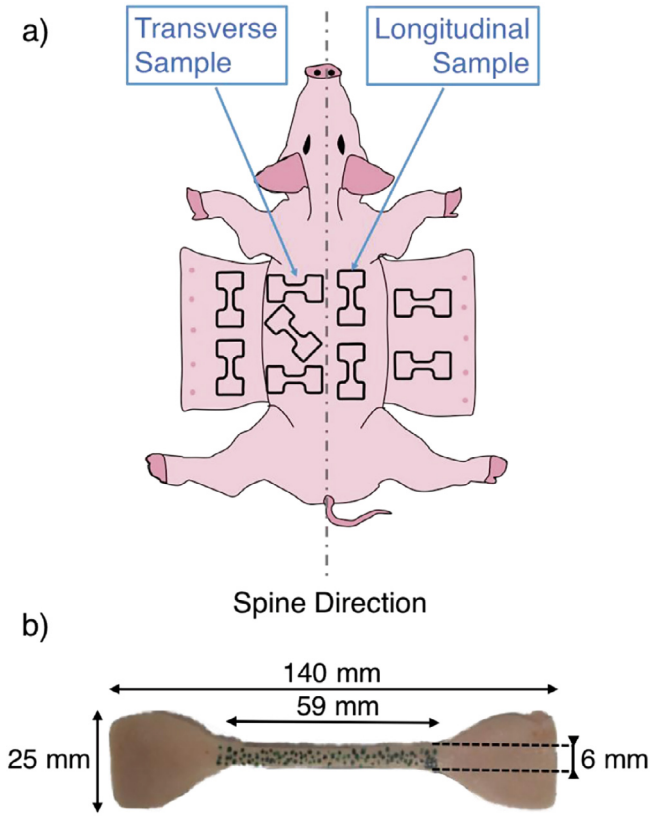

Fig. 1. (a) Tensile specimens extracted from dorsal and ventral pig skin with orientations marked. (b) Dimensions of tensile specimens cut according to the ASTMD-412-B standard for testing rubbers and elastomers [54]; reduced gage length 59 mm.

hours prior to testing, and occasionally sprinkled with water to avoid excessive drying. Testing was conducted within 3 days after the pigs were sacrificed. In California, skin was obtained already excised from a local farm (Winfield Farm, Buellton, CA, USA), and shipped overnight. Samples were prepared following the same procedure. A significant difference is that the age of the pigs was much higher (~1 year-old), a factor that is known to cause differences in mechanical properties.

2.2. Tensile setup and loading configurations

A special gripping method was used to prevent slipping of the specimen ends during testing. The assembly consists of perforated steel plates with sharp wedges, glued to wooden pads used for mounting on the testing machine. Samples were tested by using a HTE Hounsfield universal testing machine at the U. of Cambridge, and an Instron 3300 single column testing machine at UCSD. Strain-rate change, stress relaxation, and loading/unloading tests were conducted to extract fundamental parameters of deformation. No sample preconditioning was performed, to avoid generating irreversible damages to the tissue prior to actual testing.

2.2.1. Strain rate changes

A total of 30 samples were tested: 17 taken parallel to the direction of the spine (longitudinal samples), among which 14 were tested in Cambridge and 3 were tested in California, and 13 taken perpendicular to it (transverse samples), with 2 samples tested in Cambridge and 11 samples tested in California. Different crosshead speeds were imposed, resulting in strain rates of $10^{-4}\,s^{-1}$ (1 longitudinal sample), $10^{-3}\,s^{-1}$ (3 longitudinal and 2 transverse samples), $10^{-2}\,s^{-1}$ (6 longitudinal and 3 transverse samples), $10^{-1}\,s^{-1}$ (3 longitudinal and 4 transverse samples), and $0.5\,s^{-1}$ (4 longitudinal and 4 transverse samples). To further establish the influence of the strain rate on the mechanical response of skin, the crosshead speed changed in the course of a single test, increasing from $10^{-3}\,s^{-1}$, to $5{\cdot}10^{-3}\,s^{-1}$, and to $10^{-2}\,s^{-1}$ for one transverse sample, and decreasing from $10^{-2}\,s^{-1}$, to $10^{-3}\,s^{-1}$, and to $10^{-4}\,s^{-1}$ for another.

2.2.2. Stress relaxation

The viscoelastic response of skin was observed by stretching 12 samples by given increments of strain:0.1 increments – 2 transverse and 2 longitudinal samples; 0.2 increments – 3 transverse and 3 longitudinal samples; 0.5 increments – 1 transverse and 1 longitudinal samples.

The skin was left to relax for 30 s between each relaxation cycle, and the strain is incrementally raised until failure.

The obtained stress over time relaxation curves were normalized to facilitate comparison, and were then fit with a three-term Prony series, using the curve fitting tool in Matlab:

$$\frac{\sigma(t)}{\sigma_0} = a + be^{-t/\tau_1} + ce^{-t/\tau_2}$$

where σ_0 is the stress at the onset of relaxation, a, b and c are material parameters, and τ_1 and τ_2 are time constants, associated with processes occurring at different time scales. Short relaxation times were preferred so that environmental conditions such as sample dehydration, inherent to *ex vivo* testing, could not affect the viscoelastic response of the material after several cycles. As a result, longer relaxation constants (>1000 s) were not measured.

2.2.3. Loading/unloading tests

Loading/Unloading tests of 8 longitudinal samples were conducted, with initial loading interrupted at strains ε_c of 15% (2 samples) and 35% (6 samples). After one cycle, the samples were reloaded until failure.

2.3. Digital image correlation

2.3.1. 2-D mapping of the deformation on the outer surface

Digital Image Correlation (DIC) was used for an accurate estimation of strain values. The deformation process was captured using a Phantom V120 high speed camera (resolution:512 × 512; frame rates: 10 fps, 20 fps, 80 fps). The surface of the samples was speckled with dots, randomly placed using a permanent marker; a typical specimen is shown Fig. 1b. Tracking of these specific markers was then conducted. The Poisson ratio of some recorded tests (5 transverse samples, 4 longitudinal) was calculated using the Matlab DIC software Ncorr 2.1 [55]. The post-processing algorithm of the software provides average estimates of the Lagrange strains in the longitudinal/tensile direction E_{yy}, and in the lateral direction E_{xx}, over time. Using these parameters, the evolution of the Poisson ratio v can be calculated:

$$v = -\frac{\ln(\lambda_{xx})}{\ln(\lambda_{yy})}$$

where $\ln(\lambda_{ii})$ corresponds to the Hencky strain, for which the Poisson ratio remains constant for incompressible materials [56]. The stretch ratios λ_{ii} are obtained from the Lagrange strains via the following relationship:

$$\lambda_{ii} = \sqrt{1 + 2E_{ii}}$$

2.3.2. Coupling with measurements of the changes in thickness

The same setup as the one presented above was implemented for three longitudinal pig skin samples from California, except that

this time two Logitech C920 high definition webcams were used to record the deformation in the lateral direction (similarly to what was done previously) and in the thickness direction. Both cameras were mounted on flexible tripods, and a laser alignment tool was used to ensure that each objective is well aligned with the observed surface of the sample (i.e. the outer surface and the thickness section of the sample) and that they are both perpendicular to each other. A schematic illustration of the setup is presented in Fig. 2. The tested samples are mounted on the Instron 3300 and tested under tension at a strain rate of 0.01 s^{-1}, until sample failure. Samples are speckled on both sections, and the deformations are recorded synchronously via the proprietary software. Different colors were used for speckling, to facilitate the observation of out-of-plane deformations (sample flattening or curving, twisting, etc.).

From recordings obtained on both sections of the sample, all three principal stretches λ_{xx}, λ_{yy}, and λ_{zz} can be obtained. Note that both sections provide a measurement of λ_{yy}, the stretch in the tensile direction. Thus, results are considered satisfying when the error between both measurements is below 2%. From these measurements, one can also estimate the rate of volume change, given by:

$$\frac{\Delta V}{V_0} = \lambda_{xx}\lambda_{yy}\lambda_{zz}$$

where ΔV indicates the change in volume and V_0 is the initial volume of the sample.

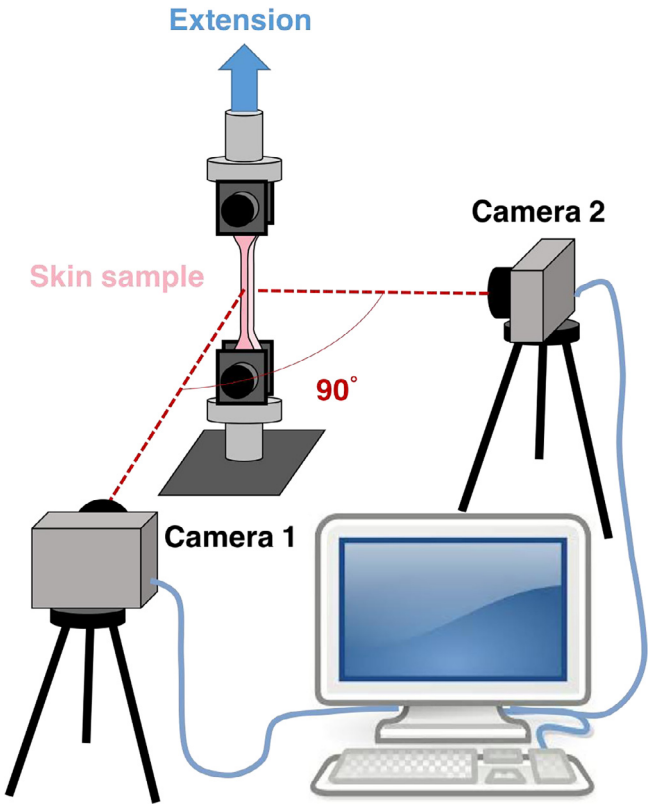

Fig. 2. Schematic description of the experimental method to estimate sample deformation in the lateral and in the thickness directions compared to the deformation in the tensile direction, using two identical cameras focused along perpendicular axes. Camera 1 monitors the deformation on the outer surface of the sample, and Camera 2 records the deformation in the thickness direction.

2.4. Imaging techniques

Scanning and transmission electron microscopy were used to establish the structure prior to and after mechanical testing (until failure). Particular attention was placed on the configuration of collagen fibers in the dermis. For enhanced tridimensional visualization of collagen in fresh skin, second harmonic imaging microscopy was also used.

2.4.1. Scanning electron microscopy

The structure of skin was fixed in a 2% glutaraldehyde solution, immediately after excision or after testing. Samples were dehydrated by consecutive immersion in 50%, 70%, 90%, and 100% ethanol solutions. Strips of skin were cut in the cross-section and parallel to the surface of the dermis using a surgical blade. The samples were then dried in a critical point dryer (Tousimis Auto Samdri 815A), and the surfaces were sputter coated with iridium (Emitech K575X). A FEI SFEG ultra-high resolution SEM was used to visualize the arrangement of the constitutive elements of skin.

2.4.2. Transmission electron microscopy

The skin was cut using a scalpel into 5 mm × 2 mm strips. Fixation was done by immersing the strips in 2.5% paraformaldehyde, 2.5% glutaraldehyde, 0.1 M cacodylate buffer for 2 h, and subsequently in 1% osmium tetroxide in 0.15 M cacodylate buffer for 12 h. The specimens were then stained in 1% uranyl acetate for 12 h and dehydrated with 50%, 70%, 90% and 100% ethanol solutions followed by a 1:1 ratio of 100% ethanol and 100% acetone, and 100% acetone (20 min immersion each time). Samples were then embedded in low-viscosity resin, starting with a 1:1 ratio of 100% acetone and resin (40 min), and finally only resin, subsequently polymerized at 48 °C for 48 h. Sections 70–100 nm thick, in all three directions of the tissue, were sliced using a Leica Ultracut UCT ultramicrotome and a Diatome diamond, and placed on copper grids for TEM observation. Post-staining with Sato lead for 1 min was performed.

2.4.3. Second harmonic imaging microscopy

A small piece (~10 mm × 5 mm × 5 mm) of fresh pig skin was placed in a dish and immersed in water, prior to mounting it on the stage of a Leica SP5 confocal microscope. Collagen emits second harmonic generation fluorescence [57] and can therefore be observed using the appropriate contrasting method with the microscope. Using a 20× water objective, the cross section of the dermis region was observed, and perpendicular slices of the sample were acquired through the depth of the tissue, with a thickness of 129.36 μm and a spatial resolution of 1.47 μm. The volume rendering of the structure allows one to gain a better visualization of the tridimensional collagenous network.

2.5. Model experiments

Human virgin black hair was purchased from an online vendor (www.s-noilite.com) and triple braids of bundles of hair of similar diameter (~4 to 5 mm) were made, in an attempt to represent the deformation process in interwoven collagen fibers. Portions of ~5 cm were cut out, and both ends were glued to sandpaper sheets with epoxy. The samples were then placed in an Instron 3300 single column testing machine for loading/unloading tests, with loading cycles interrupted at 100, 150, and 200 N.

2.6. Statistical analysis

In order to make a distinction between the effects of testing conditions and intrinsic parameters such as pig age and sample orientation, a backward stepwise multiple regression analysis was

implemented, using the Minitab 17 Statistical Software (State College, PA: Minitab, Inc). Regression models are fit to a given response parameter, using results from all tests, and a p-value is associated to each parameter, as well as a global p-value and an adjusted R-square value. For each iteration of the model, the variable with the highest p-value in the previous regression is removed. The adjusted R-square is used to assess the ability of the model to predict the expected response, and the global p-value determines whether the model should be rejected or not, using an alpha of 5%.

3. Results and discussion

The mechanical response of skin in tension is characterized by an increasing slope of the stress-strain curve; this is commonly referred to as the J-curve type of behavior, which can be encountered in many biological tissues such as tendon, arteries, and skin [10,58–61]. Fig. 3a shows the four characteristic stages of this curve, which are well known in the literature: the toe corresponds an initial extension of the tissue, at relatively low loads, followed by a hardening response with an increasing slope in the heel region, and a linear region characterized by a quasi-constant slope, which decreases at higher strains due to permanent damage, preceding failure. Some specific parameters of this tensile response, indicated on Fig. 3a, are used in this study to quantify changes with different strain rates.

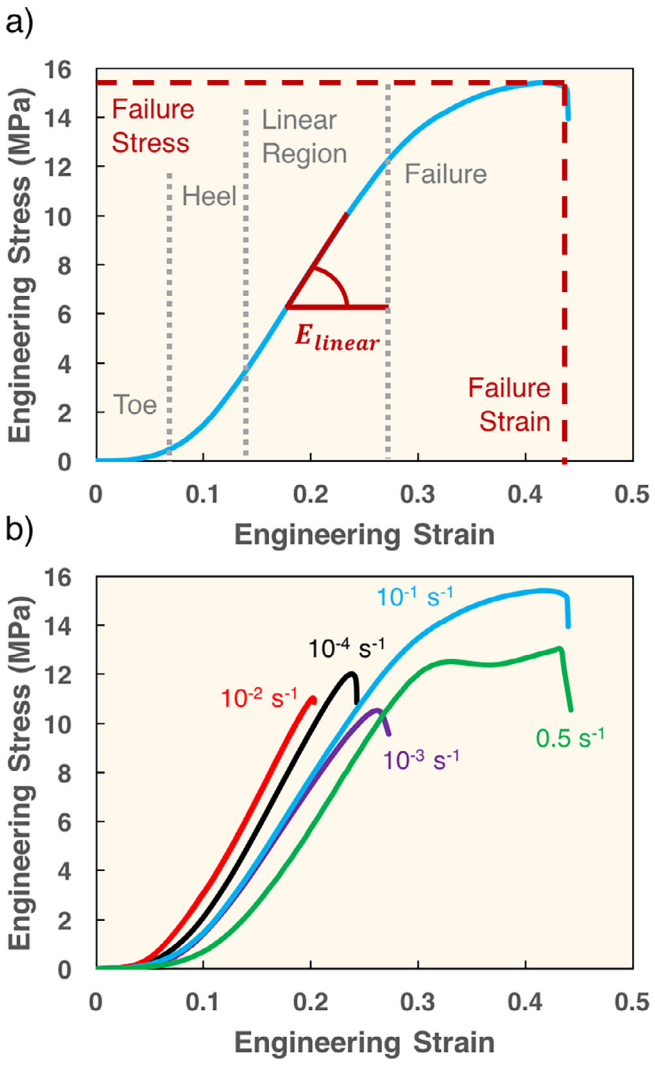

Fig. 3. (a) Four characteristic stages of the tensile response of skin: toe, heel, and linear regions, succeeded by failure of the tissue. The slope of the linear region, i.e. the tangent modulus E_{linear}, is indicated as well. (b) Effect of strain rate on tensile response of skin (characteristic curves).

3.1. Strain rate sensitivity

3.1.1. Inter-sample variations

Fig. 3b shows characteristic stress-strain curves of skin at five strain rates: 10^{-4} s^{-1}, 10^{-3} s^{-1}, 10^{-2} s^{-1}, 10^{-1} s^{-1}, and 0.5 s^{-1}. The variation between individual specimens is significant, and larger than the effect of the strain rate. Thus, it is difficult to directly observe the strain-rate sensitivity of skin from separate tests. It will be later shown that strain-rate change tests on a single specimen are more appropriate. To ease comparison between individual specimens, four parameters were extracted from the stress-strain curves to compare the effect of strain rate, as well as the effect of sample orientation; namely the failure strain, the failure stress, the modulus of the linear region (sometimes referred to high strain modulus or 'Young's' modulus in the literature), as well as the stress at the transition between the heel and the linear regions (see Fig. 3a). The latter was determined by estimating the stress at which the derivative of the stress-strain curve transitions into a horizontal plateau region. The results are plotted in the bar charts of Fig. 4. Red columns represent transverse sample orientation (perpendicular to spine direction), and blue columns correspond to the longitudinal orientation (parallel to spine direction). Moreover, because of the different sources of tested samples, the combined influence of orientation, strain rate, and pig age on all four parameters was studied in more detail by conducting a stepwise multiple regression (see Section 2.6). Results are presented in Table 1.

There is no significant effect of either orientation, strain rate, or age on the failure strain, which nonetheless shows a wide variability, and no model is able to accurately predict it based on these parameters and the obtained results. Ankersen et al. [45] showed that for dorsal pig skin, the level of anisotropy is significantly lower than in the belly region, where stretches in the transverse direction can go up to 1.8, vs. ~1.3 in the longitudinal direction. The failure stress and the tangent modulus both are strongly influenced by sample orientation (with respective p-values of 0.04 and 0.02 for orientation in the best regression models). The influence of strain-rate is less evident, with p-values of 0.062 for failure stress and 0.132 for the linear region modulus, slightly above the 5% limit of rejection, however neglecting their effect considerably reduces the accuracy of the prediction, as shown by the adjusted R-square values. Age does not appear to have a notable impact on these variables. These results corroborate the findings of Ottenio et al. [41] on the strain-rate sensitivity of dorsal human skin, where similar trends were reported for three strain rates. The stress at the onset of the linear region appears to be highly related with the age of the pig, with p-values below 0.001 for this parameter. The effect of orientation was rejected, however including the influence of the strain rate results in a slightly better prediction (a higher adjusted R-square), an effect that is also observable on the histograms in Fig. 4d, suggesting that strain rate impacts viscoelastic and rearrangement processes.

3.1.2. Sequential changes of the loading rate

Strain-rate change tests were conducted for individual specimens, by both increasing or decreasing it in the linear region of the J-curve according to the following sequences: 10^{-3} s^{-1}-$5{\cdot}10^{-3}$ s^{-1}-10^{-2} s^{-1} and 10^{-2}s^{-1}-10^{-3} s^{-1}-10^{-4} s^{-1}. There is no jump in the stress when the strain rate is increased by a factor of 5 or 10 (Fig. 5a); this is different from the response of metals [62], in which an instantaneous increase in stress is observed by virtue of the dependence of dislocation velocity on stress, as expressed by the Orowan equation. However, an increase in the tangent modulus

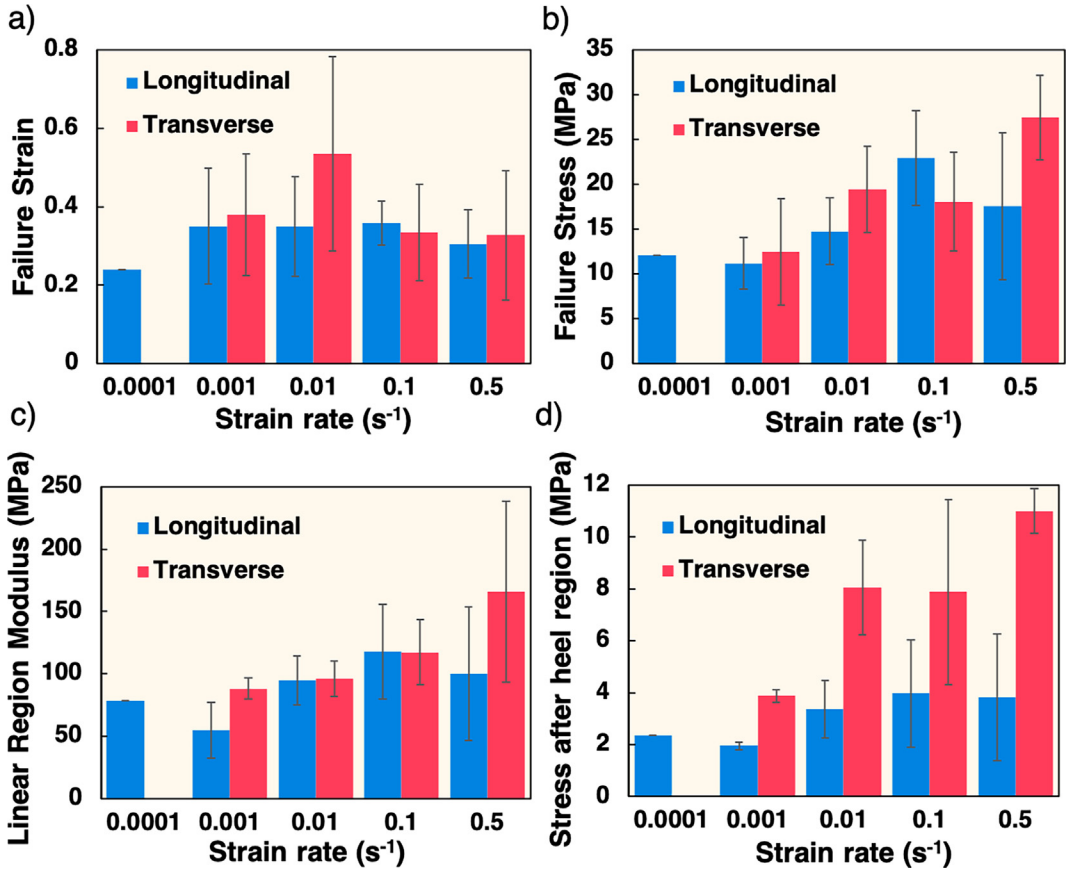

Fig. 4. Tensile response parameters in longitudinal and transverse specimens removed from dorsal region, parallel and perpendicular to the direction of the spine. While failure strain (a) is not affected by strain rate, the failure stress (b), the tangent modulus in the linear region (c), and the stress level after the heel region (d) (beginning of linear region) increase with strain rate. Differences between longitudinal and transverse samples are not very significant in the dorsal region, but a generally higher level of stress after the heel region is observed for transverse samples.

Table 1
Multiple regression analysis of the influence of sample orientation, strain rate, and pig age on failure strain, failure stress, linear region modulus, and stress at the transition between the heel and the linear region. For each multi-parameter stepwise model, the global p-value, the p-value of each individual variable, and the adjusted R-square are provided. The asterisk (*) corresponds to a parameter that is omitted in the model. The best model for each response is highlighted in grey.

Parameter	p-value				Adjusted R-square
	Model	Orientation	Strain-rate	Age	
Failure strain	0.153	0.209	0.445	0.060	8.58%
	0.093	0.130	*	0.031	9.92%
	0.116	*	*	0.116	8.57%
Failure stress	0.046	0.135	0.077	0.994	17.62%
	0.017	0.040	0.062	*	20.67%
	0.030	0.030	*	*	15.73%
Linear region modulus	0.040	0.185	0.114	0.563	18.55%
	0.017	0.020	0.132	*	20.54%
	0.015	0.015	*	*	16.53%
Stress at heel	0.002	0.220	0.167	0.048	36.69%
	0.001	*	0.083	<0.001	35.33%
	0.001	*	*	0.001	32.57%

can be observed in the linear region, with values rising from 39.9 MPa, to 79.1 MPa and finally 86.8 MPa. For the decrease in strain rate, a small drop was observed (Fig. 5b): there is relaxation in the specimen due to lower dynamics of the deformation, and the decrease in modulus is less pronounced, with measured values of 14.3 MPa, 14.8 MPa, and finally 11.0 MPa. This change in slope and stress drop with decreasing strain rate are viscosity effects, dictated by microscale time-dependent phenomena such as interfibrillar shear and the intrinsic viscosity of the ground substance.

3.2. Evolution of the Poisson ratio and influence of sample orientation

Some steps of the method to calculate the Poisson are presented Fig. 6a–d, and the evolution of the Poisson ratios with the applied

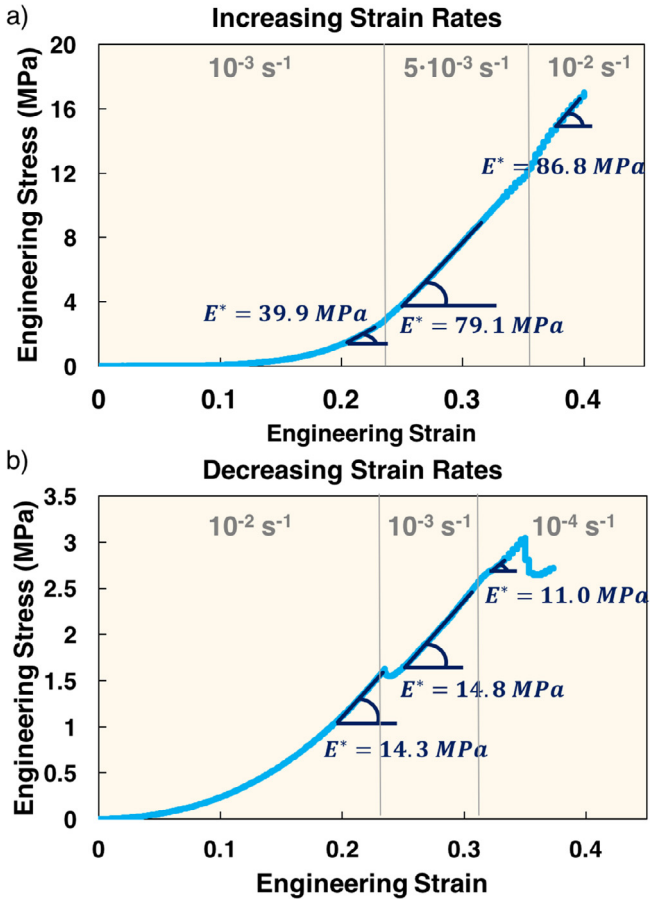

Fig. 5. Tensile tests of longitudinal samples of pig skin with changes of the strain rate in the linear region of the stress-strain cruve; (a) strain rate increase; (b) strain rate drop.

stress is plotted Fig. 6e. During tension, the Poisson ratio of skin is not constant, and stays mostly outside of the range of traditional isotropic incompressible materials (where it is limited by 0.5). Fig. 6c shows that, for a longitudinal sample, a rough estimation of the ratio between lateral expansion and tensile stretch can reach approximately 1: $(6.46/5.86)/(16.77/15.62) \approx 1.03$. This would result in a Poisson ratio around −1.4, which is close to the lowest values displayed in Fig. 6e. An interesting observation is that the initial evolution of the parameters is dictated by sample orientation: longitudinal samples start with negative values at low stresses, mostly around [−1; −0.5], and gradually increase, converging towards 0.5, the limit of incompressibility of isotropic rubber-like elastomers. Inversely, transverse samples have their initial Poisson ratio around 1 or above, as in the work of Lees et al. [51], and decrease towards 0.5 with increasing tensile stress. This effect of skin anisotropy on the Poisson ratio is reported herein for the first time, to our knowledge. It is likely that differences in the process of rearrangement of collagen fibers, with different initial orientations, affects lateral contraction of the samples, and therefore the Poisson ratio. The significant differences in values at low stresses can be related to different levels of anisotropy for each sample, which were taken from different regions of the body. Data from measurements in both directions, as described in Section 2.3.2, can be useful to estimate the other Poisson ratio in the thickness direction (ν_{yz}), volume changes, and sample distortion. Experimental results are summarized in Fig. 7. Fig. 7a and b show the 2D strain maps from which the average stretches are obtained. It can be observed that deformations in the thickness direction appear more heterogeneous, although the obtained average in the tensile direction is roughly the same. No torsion, flattening, or curving is observed during deformation. The region of interest of the DIC processing stays within the observed section of the sample. Note that each sample (1,2,3) was taken with the same orientation, but each time further away from the spine. A direct consequence is that a change in tissue anisotropy due to body region is directly observable in the experimental results, as seen on the stress-strain curves Fig. 7c. Trends of the Poisson ratio in the lateral direction ν_{yx} (Fig. 7d) are slightly affected as well, but most importantly the initial offset of the evolution curve is different and decreases the closer one gets to the belly region, which is where most of the previous samples where tested. This time, the Poisson ratio in the thickness direction ν_{yz} can be observed as well (Fig. 7e): the opposing trend is seen for the initial offset, with values increasing as one gets further from the spine. Sample 1 shows an initial coefficient close to −0.8, indicating that negative Poisson ratios are also found in this direction. Interestingly, sample 2 starts from 0.5 but decreases towards negative values, reaching a final coefficient around −0.15, suggesting that these are not strictly limited to the reference state. This also implies that after a certain applied stress, the sample starts swelling in the thickness direction: this evolution is further detailed in SI I. As a matter of fact, considerable swelling can be observed for sample 1 (up to 5%) and sample 2 (up to 15%), as reflected by the evolution of $\Delta V/V_0$ (Fig. 7f). Sample 3, which does not show a negative Poisson ratio, has a more stable evolution of the volume ratio, with a slight initial drop (<5%), suggesting some loss of volume.

In order to test the accuracy of the method, we conducted similar tests with samples of layered thermoplastic rubber, for which the mechanical properties are more consistent. Results are available in SI II. From these tests, we conclude that some inaccuracies are inherent to the method itself, due to limitations in resolution, especially at low strains. However, good reproducibility and accuracy at larger stresses are reached in general.

Moreover, a uniaxial tensile setup is not sufficient to fully characterize the anisotropic deformation of the tissue [25,63]. Some complimentary Poisson ratios cannot be measured with this method, and additional degrees of freedom limit the precision of the indirect measurements. No influence of the strain rate on the Poisson ratio has been observed from our measurements.

3.3. Stress-relaxation

Three normalized relaxation cycles of a longitudinal and a transverse skin sample are presented Fig. 8a and b. For each cycle and orientation, similar values of the stress before relaxation were isolated to facilitate comparison, namely approximately 1 MPa, 4 MPa, and 6 MPa. Prony series least-squares fit are also plotted, and generally show a high R-square coefficient, above 0.99. With increasing applied stress, the elasticity modulus at the end of the relaxation period increases, which is expected for a non-linear material with a J-shaped stress-strain curve, and thus an increasing tangent modulus. The moduli are higher for the transverse samples, as observed previously for strain-rate sensitivity tests. Further details on the relaxation times can be extracted from the evolution of the Prony series parameters with applied stress, presented Fig. 8c–f for the two samples that were selected. The time constant τ_1 (Fig. 8c) remains within the order of magnitude of 10 s. Rather similar trends are observed between longitudinal and transverse samples: the relaxation constant increases with tensile stress, stabilizes near the linear region of the sample, and decreases at the onset of damage, close to failure. The smaller time constant τ_2 (Fig. 8d) is in the range of ∼1 s, and follows a similar trend. Values for both constants are slightly higher for the transverse sample than for longitudinal one. The difference between the two time constants could come from the existence of mesoscale constituents with different viscos-

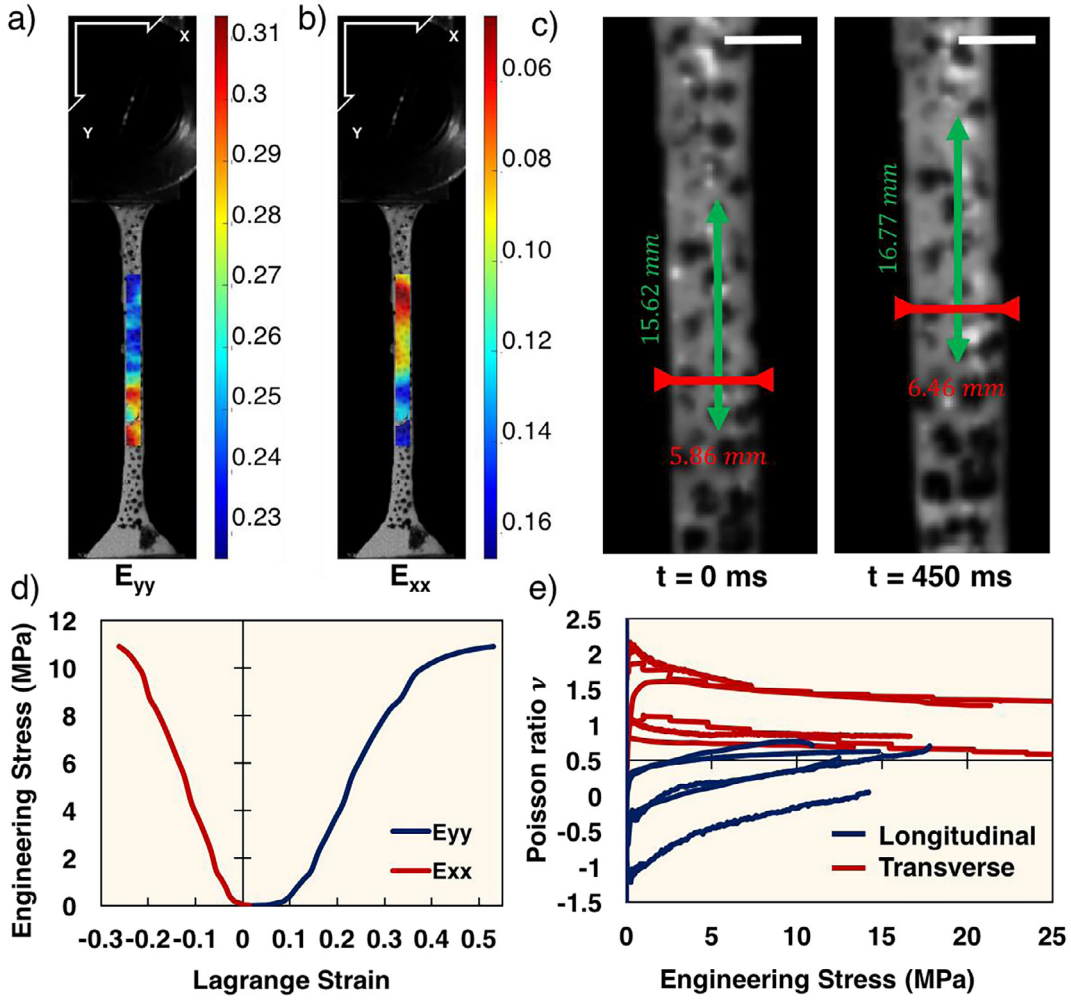

Fig. 6. Post processing of recorded experiments by Digital Image Correlation (DIC). Local Lagrange strain maps in the vertical/tensile direction (a) and in the horizontal/lateral direction (b). (c) Manual measurements of two-point distances in the lateral and tensile direction in the initial configuration (t = 0 ms) and during deformation (t = 450 ms) at 0.5 s^{-1} of a longitudinal sample show that lateral expansion is almost equivalent to the tensile stretch (white scale bars = 5 mm). (d) Local strains can be averaged to obtain the macroscopic deformation, and thus stress/strain curves in both directions. (e) Calculated Poisson ratio using post-processed DIC of 5 longitudinal samples and 6 transverse samples, plotted against applied stress. Results show a different evolution according to sample orientation, symmetric around 0.5, which is the incompressibility limit.

ity and elasticity, in which case the soft viscous matrix would have a smaller relaxation time constant. Another possibility, suggested by Emile et al. [64] for spider dragline silk and by Yu et al. [65] for hair, is that each time constant corresponds to a different hierarchical level of the structure (nested model). We can hypothesize that the relaxation constants are due sliding processes occurring at the fiber level (τ_1) and at fibril level (τ_2), and longer time constants, associated with slower mechanisms in the tissue, can be identified with longer relaxation times. This would require the expansion of the Prony series to additional terms, and would modify also the previous values. Nonetheless, the consistency between experiments was favored, with similar relaxation times and function parameters, so that a compatible analysis can be performed. Parameters of the fitting function were limited to 5 to ease the comparison, and also because with a relaxation of 30 s and a time resolution of ~1 ms, identifiable time constants are constrained within this range. A notable difference between the transverse and the longitudinal reduced modulus a is seen Fig. 8e, which could also be expected from the difference in elastic modulus reported earlier. Parameters b and c are within the same range, and decrease with applied stress, with this time higher values for the longitudinal sample. This trend is explained by the fact that for any applied stress $\sigma(0)/\sigma_0 = a + b + c = 1$, and with the increasing trend of a.

Table 2 provides values of all the Prony series parameters taken for all the relaxation tests that were conducted. Only parameters taken from the stable region, the linear region of the J-curve, were used in the calculation of the average, to reduce data scattering. As a result, very consistent parameters were obtained, with small standard deviations, regardless of inter-sample and intra-sample variations. The p-value between transverse and longitudinal samples for each parameter was determined with a paired t-test, and show very significant differences for a, b, and τ_1, similarly to what was found in the comparison of the first two samples. The p-value of parameter c is slightly above 1% (p-value = 0.018), and no significant difference can be inferred on the values of the associated time constant τ_2. This suggests that there is a subset of constituents of the material, with low viscosity, that is less influenced by tissue anisotropy. However, all calculated average values are very close to each other, implying a rather low influence of sample orientation on the relaxation response of skin.

3.4. Cyclic testing and damage evolution

Viscoelasticity of skin is also demonstrated by the hysteresis stress-strain curve followed during sequential loading and unloading of samples in tension, as can be seen in some results presented

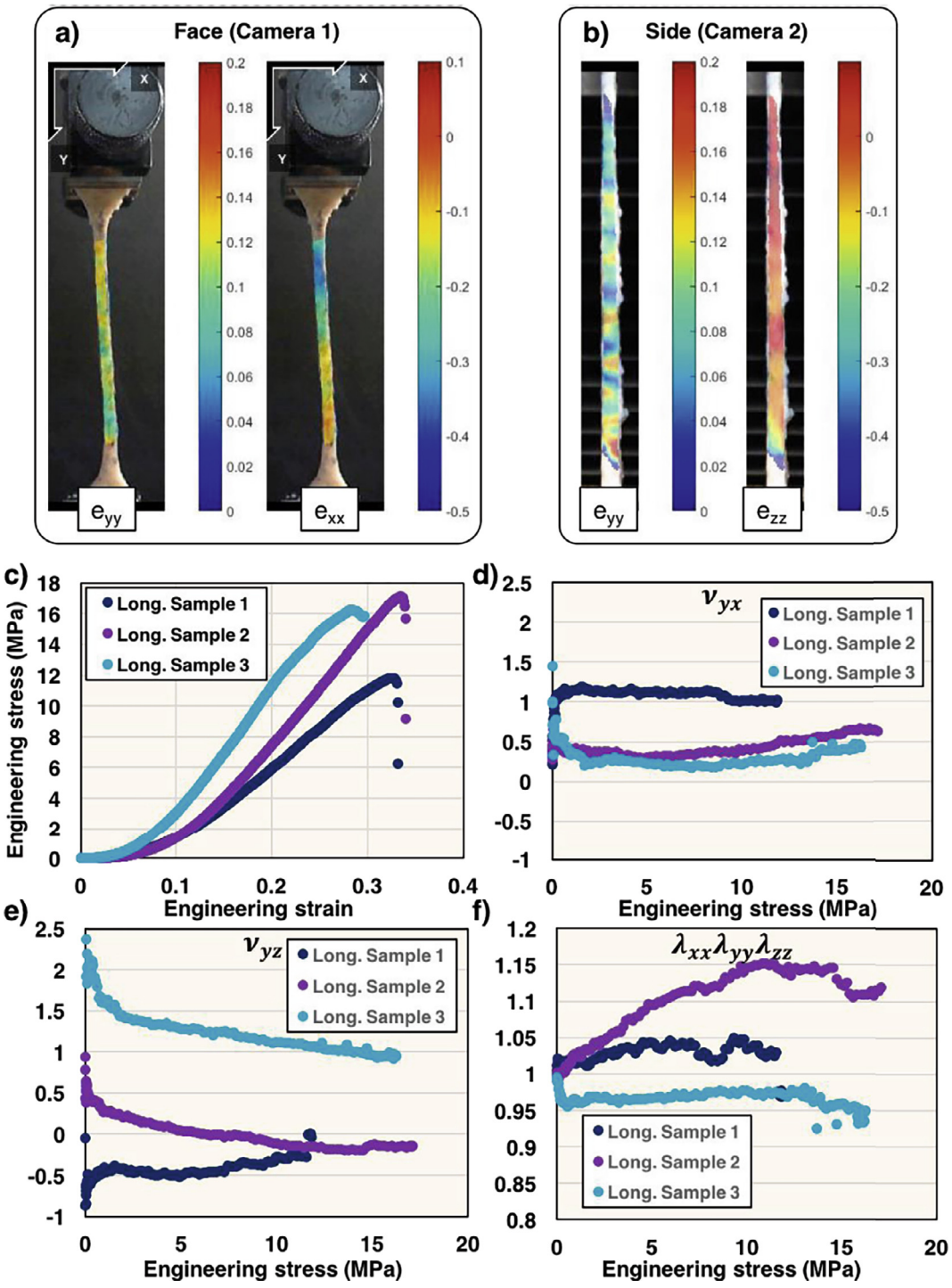

Fig. 7. (a) Euler-Almansi strain maps from DIC post-processing in the tensile (yy) and lateral (xx) directions at a macroscopic stress level of 2.3 MPa for a pig skin sample. (b) Euler-Almansi strain maps in the tensile (yy) and thickness (zz) directions at the same stress level for the same sample. (c and d) Evolution of the Poisson ratios ν_{yx} (b) and ν_{yz} (c) with applied tensile stress for the three longitudinal skin samples that were tested. Results show large variations and high tissue anisotropy, with values spanning approximately −0.5 to 2. (e) Rate of volume change with applied stress. Trends indicate significant changes in volume depending of the region from which the sample was taken.

Fig. 9a. The existence of remnant strains after unloading shows the establishment of a new equilibrium position, a result of irreversible changes occurring in the structure [42,66,67]. Experimental observations [8] have also shown that upon reloading, skin follows the same path as the unloading curve, a phenomenon called the Mullins effect (not presented here).

The area contained inside the hysteresis curve, equal to the viscoelastic dissipated energy E_d, was calculated. When compared to the stress at the end of the loading cycle for each sample (Fig. 9b), the energy appears to follow very closely a power law; the least-square function that was found is $E_d = 0.017\sigma_l^{1.5279}$, with a high R-square coefficient of 0.96. This

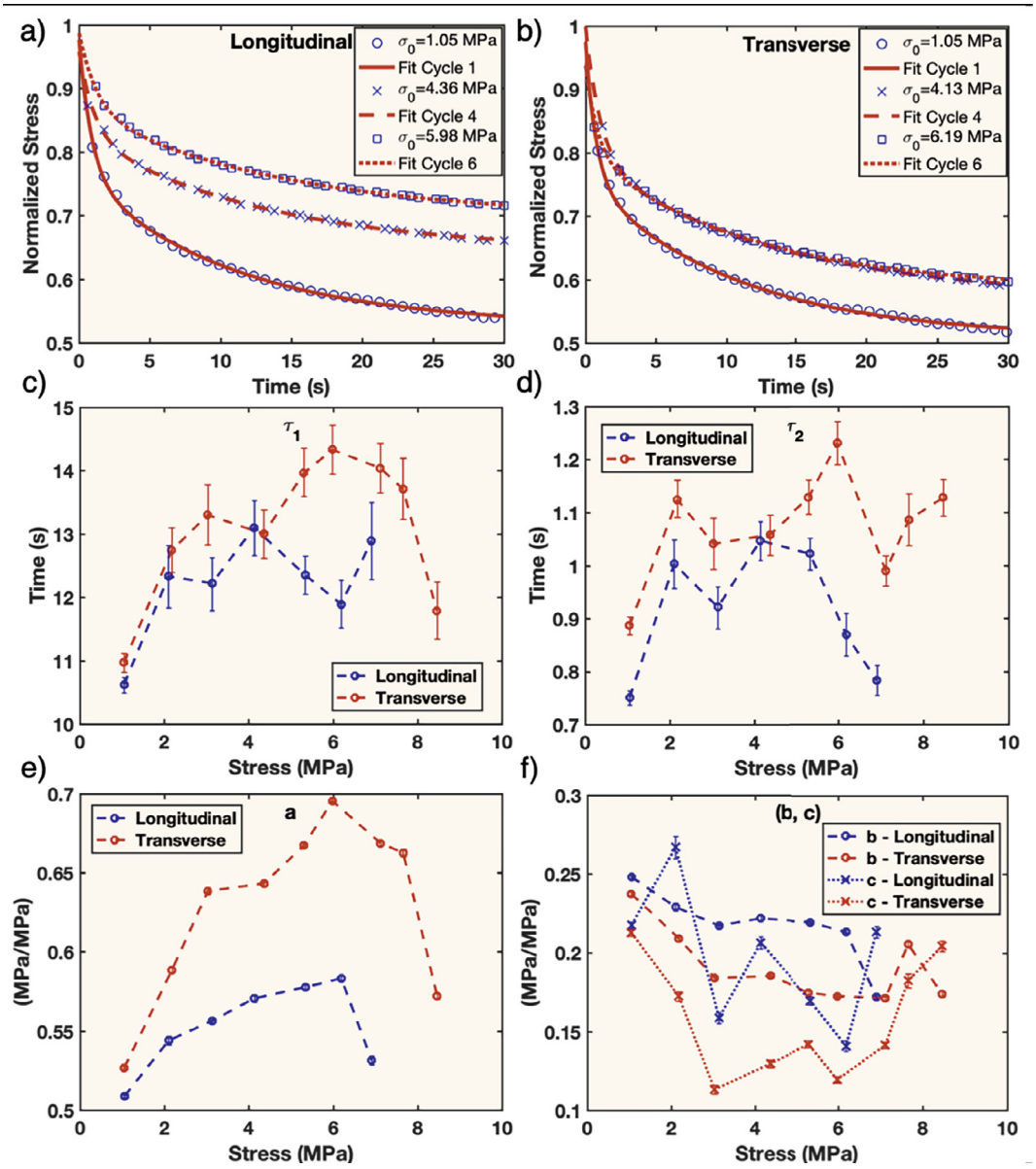

Fig. 8. Normalized stress relaxation curves of (a) a longitudinal sample and (b) a transverse sample of pig skin. Experimental results are in blue, and red lines correspond to Prony series fits. Relaxation rounds were taken for samples tested around the same stresses to facilitate comparison. (c–f) Parameters of the Prony series relaxation function: time constants (c) τ_1 and (d) τ_2, (e) normalized elastic modulus a, and (f) material parameters b and c. Errors bars in (c–f) correspond to the 95% confidence bound of the Prony series fits. The longitudinal and the transverse samples show similar evolutions of the material parameters, with a notable difference of the modulus a, as the first curves suggested. (For interpretation of the references to colour in this figure legend, the reader is referred to the web version of this article.)

Table 2
Average values of the Prony series parameters compared between longitudinal and transverse sample orientations, with standard deviations. For each orientation, parameters are averaged regardless of inter-sample and intra-sample variations, for initial relaxation stresses between 2 MPa and 10 MPa. The p-value between longitudinal and transverse samples is also reported, (*) indicates a significant variation between parameters ($p < 0.05$) and (**) corresponds to a very significant variation ($p < 0.01$).

	Longitudinal (N = 16)	Transverse (N = 22)	p-Value
a	0.580 ± 0.042	0.618 ± 0.041	0.009 (**)
b	0.223 ± 0.017	0.204 ± 0.023	0.0087 (**)
c	0.173 ± 0.037	0.145 ± 0.030	0.018 (*)
τ_1	12.102 ± 0.925	13.784 ± 1.670	0.0009(**)
τ_2	1.057 ± 0.148	1.052 ± 0.114	0.91

implies that the dissipated energy is fully determined by the stress at the end of loading (for the longitudinal orientation), and that a stress-based criterion can facilitate inter-sample comparison, for which the data is usually scattered due to large variations in biological samples. This was also observed for the comparison of the Poisson ratio (see Fig. 6d). Fig. 9c shows the evolution of the Poisson ratio of one sample during one loading/unloading cycle: the loading evolution is typical of longitudinal samples, with an initial coefficient starting at −0.5, increasing and converging towards 0.7 at the end of tension. Interestingly, the value of the Poisson ratio at unloading follows a different path, and stagnates around 0.7 all the way until the new equilibrium position. A more complete description of the

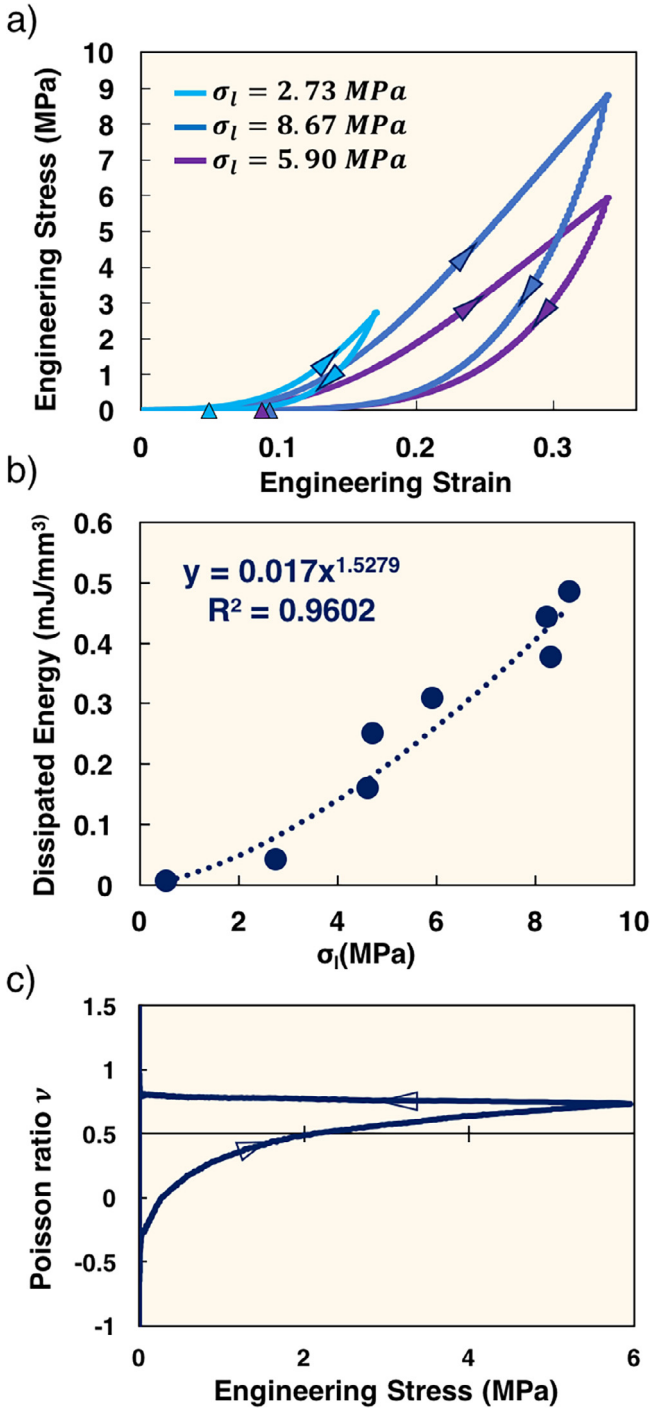

Fig. 9. (a) Loading/unloading tests of pig skin interrupted at different stresses σ_l. Arrows indicate the remnant strain ε_r for each test. The integral of the hysteresis curve, i.e. its area, is equal to the dissipated viscoelastic energy. When plotted against σ_l (b), it appears to follow a power law trend with an exponent close to 3/2, as shown by the least-squares fit on the graph, with an R-square coefficient of 0.96. (c) The Poisson ratio, calculated using the DIC post-processing method, also follows a different path during loading and unloading of the sample. Arrows indicate the evolution of the coefficient. During unloading, it remains constant around 0.78, suggesting a constant lateral expansion, above the limit of incompressibility.

evolution of the Poisson ratio during loading/unloading is provided in SI III, showing that the coefficient can also go back to, or reach, negative values for some samples prior to reloading, a trend that has also been found in fiber reinforced composites [68]. This evolution is another indication of the irreversibility of the deformation, and of an internal rearrangement of the constitutive elements of skin. More detailed insight into the process of realignment of collagen in the dermis during tension is presented in the following sections.

3.5. Ex situ imaging of collagen fiber rearrangement

The principal method of characterization used was transmission electron microscopy, which was supplemented by scanning electron microscopy and second harmonic generation microscopy. These combined techniques enable a complete tridimensional picture of the collagen arrangement and its evolution prior to testing and after sample failure.

3.5.1. Initial structure

The initial structure was imaged along three orientations: longitudinal, transverse, and in-plane. These are shown in Fig. 10. The three planes form an orthogonal set and enable visualization of the principal features. One observation that is of high relevance is that the wavy pattern characteristic of collagen is observed in all three sections. Thus, the fibers (with an average diameter of ~3 μm) are not constrained to one plane, but form a tridimensional pattern. These fibers are seen in the longitudinal (Fig. 10a), transverse (Fig. 10b) and in-plane (Fig. 10c) sections. Each collagen fiber is composed of fibrils with diameters of ~80 nm, bundled together. Ground substance (proteoglycans) fills the gap. Detailed images of the collagen fibrils are shown in the out-of-plane direction in Fig. 10d and in the in-plane direction in Fig. 10e and f. The characteristic band pattern of 67 nm of collagen is observed [10]. Fig. 10f. shows in detail the change of orientation at the fibrillar level; where collagen in-plane fibrils transition from semi-circles into ellipses, as their angle with the viewing plane increases, until reaching 90° at which orientation the cross-section becomes circular, as in Fig. 10d.

The diameters, areal fraction, and fibril density were measured and the quantified results are shown in Fig. 11. There is some variation, but the average numbers represent fairly well the distribution of sizes. Fig. 11a shows the cross-section of one prominent fiber, which was isolated and binarized as shown in Fig. 11b, to enable quantification. The fiber thickness was estimated by assimilating the cross-sectional area of a fiber to the one of a circle, and data was complemented by direct in-plane measurements of fiber thickness, from other micrographs. Very similar distributions were obtained, converging to a mean value of 2.2 μm (Fig. 11c). The distribution of the areal fraction of fibrils inside a fiber is provided in Fig. 11d, and was measured by calculating the area of black pixels (fibril) divided by the total cross-sectional area of the fiber; the rest (white pixels) is ground substance. The mean value is 0.69, compared to a theoretical maximal value of 0.85, if one assumes a close packed arrangement of cylinders inside a circle. The fibril diameter (Fig. 11f) shows some variation (see also Fig. 10d), the mean being 82 nm, consistent with previous observations of collagen in other mammals [10].

Notable by its absence is elastin. It is known that it comprises a much lower fraction of the dermis (2–4%) than collagen (~70%). It is possible that the osmium tetroxide staining does not reveal it, but it is still puzzling that it does not seem to play a significant role in the architecture of the dermis, although it is often reported as essential to the ability of skin to reversibly recoil under low strains [26]. Confocal microscopy seems to be a more appropriate tool to reveal the arrangement of elastin in the dermis, with nonetheless very low volume fractions [69].

3.5.2. Structure after failure

Extension of skin in tension to failure changes the configuration of collagen fibers significantly [4,19]. In the same way as for Fig. 10,

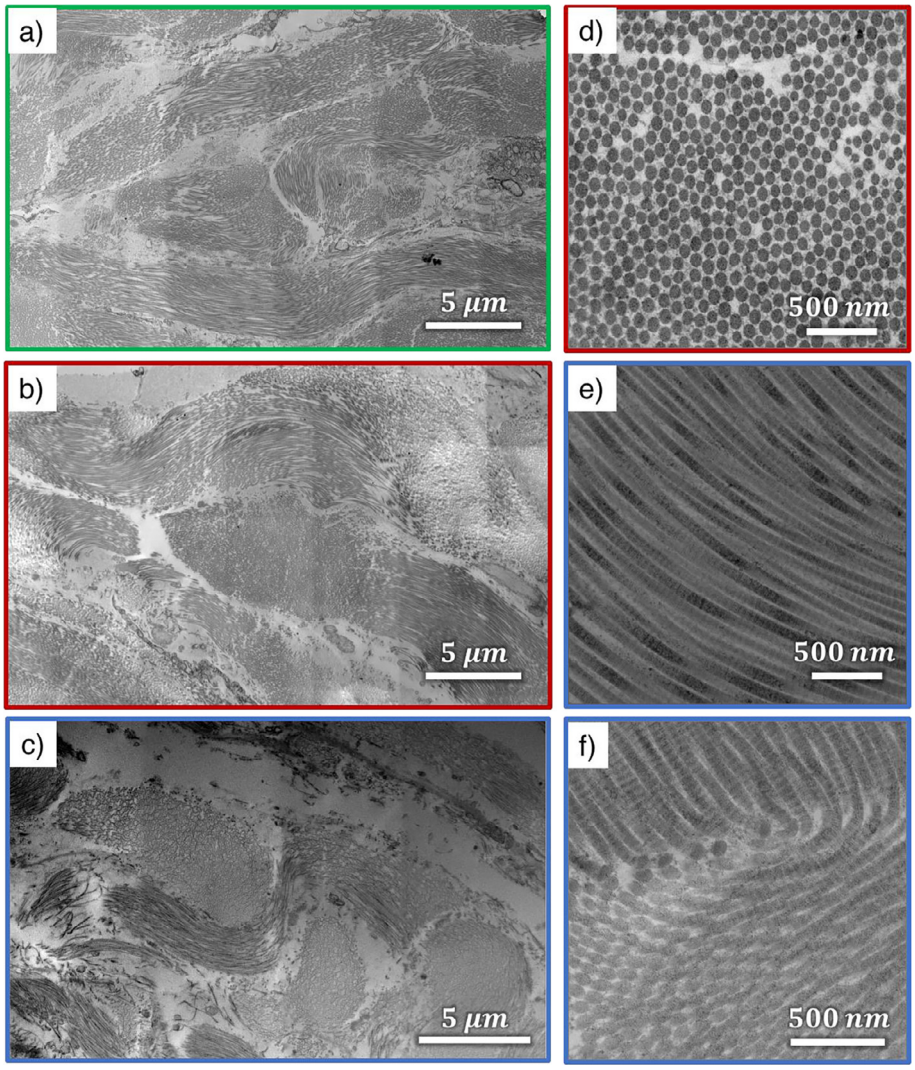

Fig. 10. Transmission electron micrographs showing the configuration of collagen in untested skin viewed in three orientations; (a) longitudinal, (b) transverse, and (c) horizontal (parallel to the outer surface) sections. Note the tridimensional weave pattern of collagen fibers. (d) High magnification transverse section of the dermis, showing collagen fibrils bundled in a fiber, going out of plane. Fibril diameter and area fraction can be estimated here. (e and f) High magnification horizontal sections of the dermis showing characteristic 67 nm d-bands of collagen fibrils, bundled together in fibers. Fibers come in and out of plane, as seen here by changes in the cross-section of collagen fibrils, from circular, to elliptical, to in-plane.

TEM was used to image the three sections (longitudinal, transverse, and in-plane). Fig. 12 shows low and high magnification views where the decrease in the curvature of the fibers is evident. The presence of interwoven fibers aligned with the three planes, is again observed. An increased alignment of the fibers with the tensile direction is seen as well, with a higher proportion of fibers confined in-plane (Fig. 12a and b), and the transverse section showing mostly out-of-plane fibers (Fig. 12c and d). Fig. 12e and f show fibers with a much smaller wavelength than in the original state; this is thought to be due to the recoil of the sample after tensile failure. Quantitative measurements of the fiber alignment, which for the longitudinal and in-plane sections corresponds to the angle between the principal axis of a fiber and the tensile direction, and is the angle between the principal axis of a fiber and the direction orthogonal to the surface of the skin in the transverse direction, are reported before testing and after sample failure in Fig. 13. Fig. 13a describes the three principal directions previously defined with respect to the tensile direction (OX_2), which coincides here with the direction of the Langer lines, and the angles (α, β, γ) used to determine the main orientation of fibers. Namely, the plane (X_1, X_2) defines the dermis surface, (X_1, X_3) defines the transverse plane (perpendicular to the tensile load and to the Langer lines), and (X_2, X_3) is the longitudinal plane. The statistical data before testing and after failure are presented in Fig. 13b–d. After failure, an increased alignment of the fibers with the tensile direction (0°) is seen, notably with a narrower distribution peak, for the dermis surface section. The same effect is observed in the longitudinal section, as collagen fibers are recruited into the tensile direction, with a decreased value of γ. In the transverse section the migration of fibers occurs towards $\beta = \pm 90°$ (Fig. 13c); this implies an increased in-plane confinement, as already observed Fig. 12c and d.

3.5.3. Collagen deformation

The radii of curvature r and the opening angles, based on a semi-circular one-dimensional model of wavy collagen fibers previously proposed by Yang et al. [19], were measured to quantify the expected straightening of collagen fibers after failure. This is shown in Fig. 14a. Statistical data for both parameters (r and ω),

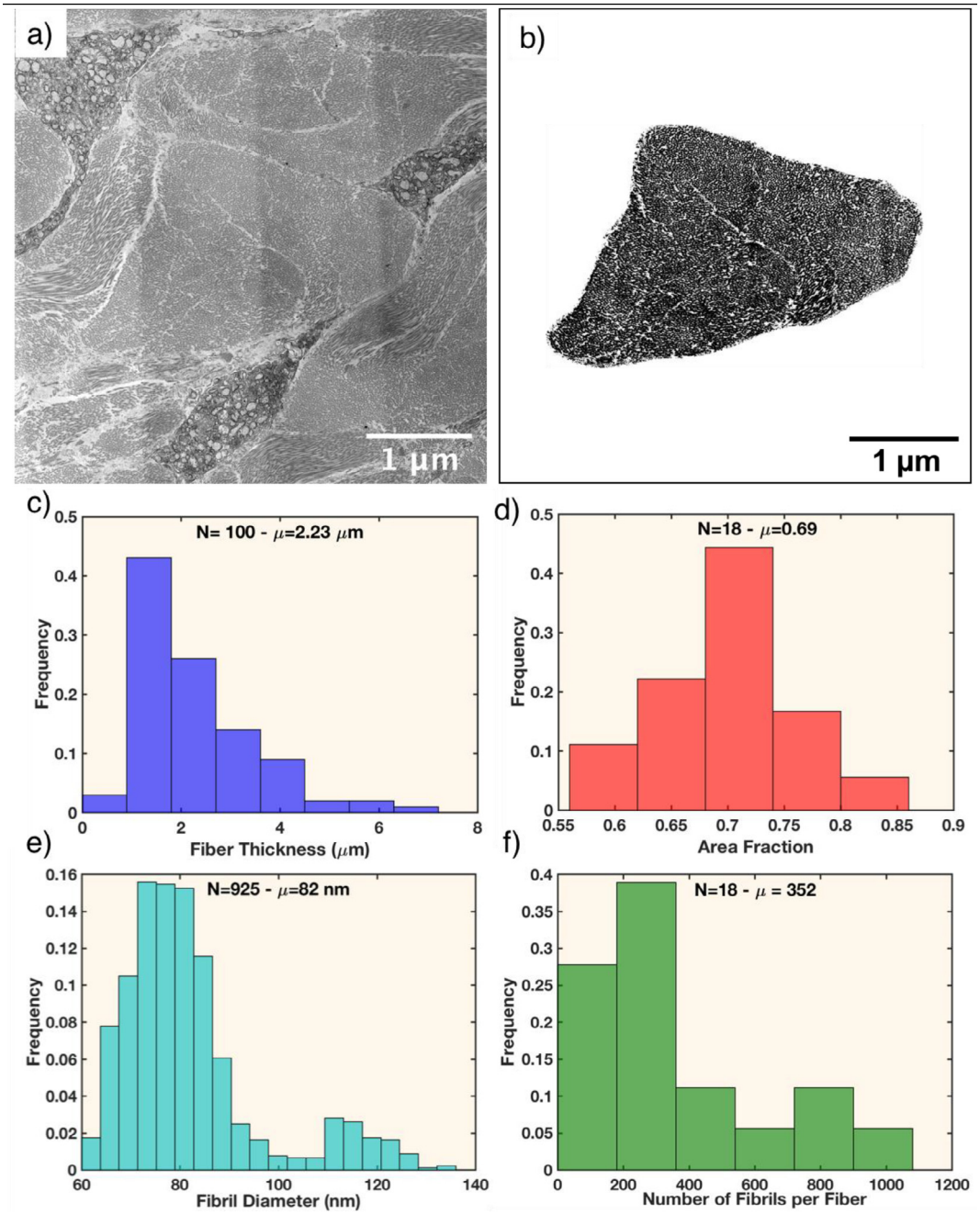

Fig. 11. (a and b) Out-of-plane collagen fibers are cropped out, and a threshold is applied to the region to isolate fibrils from the surrounding ground substance, allowing for the calculation of dimensions and area fractions. (c) Distribution of collagen fiber thickness. (d) Distribution of the area fraction of collagen fibrils contained in a fiber, centered around 0.69, below the theoretical maximum value of 0.85. (e) Distribution of collagen fibril diameters. (f) Estimation of the number of collagen fibrils per fiber. N indicates the number of elements that were used for each calculation, μ is the mean value of the distribution.

measured before testing and after failure, are reported Fig. 14b and c. It is expected that during deformation, the radius of curvature of every fiber increases, while the opening angle decreases with fiber straightening. The case of a fully taut fiber corresponds to an infinite radius and an opening angle of 0°. Statistical distributions of r and ω show the opposite trend: the radius of curvature significantly decreases, while the opening angle increases. This result can be explained by fiber recoil after sample failure or extraction, as previously observed in Fig. 12. Moreover, even though electron micrographs show more straightened fibers, measuring a radius close to infinity is not straightforward, while second order crimps are easier to quantify. A configuration with some interweaving, or braid-like structure can also explain this post-failure recoil, with neighboring fibers being less subjected to confinement between each other.

3.6. Interweaving of collagen fibers

The tridimensional nature of the collagen fiber configuration was evaluated by confocal and scanning electron microscopy.

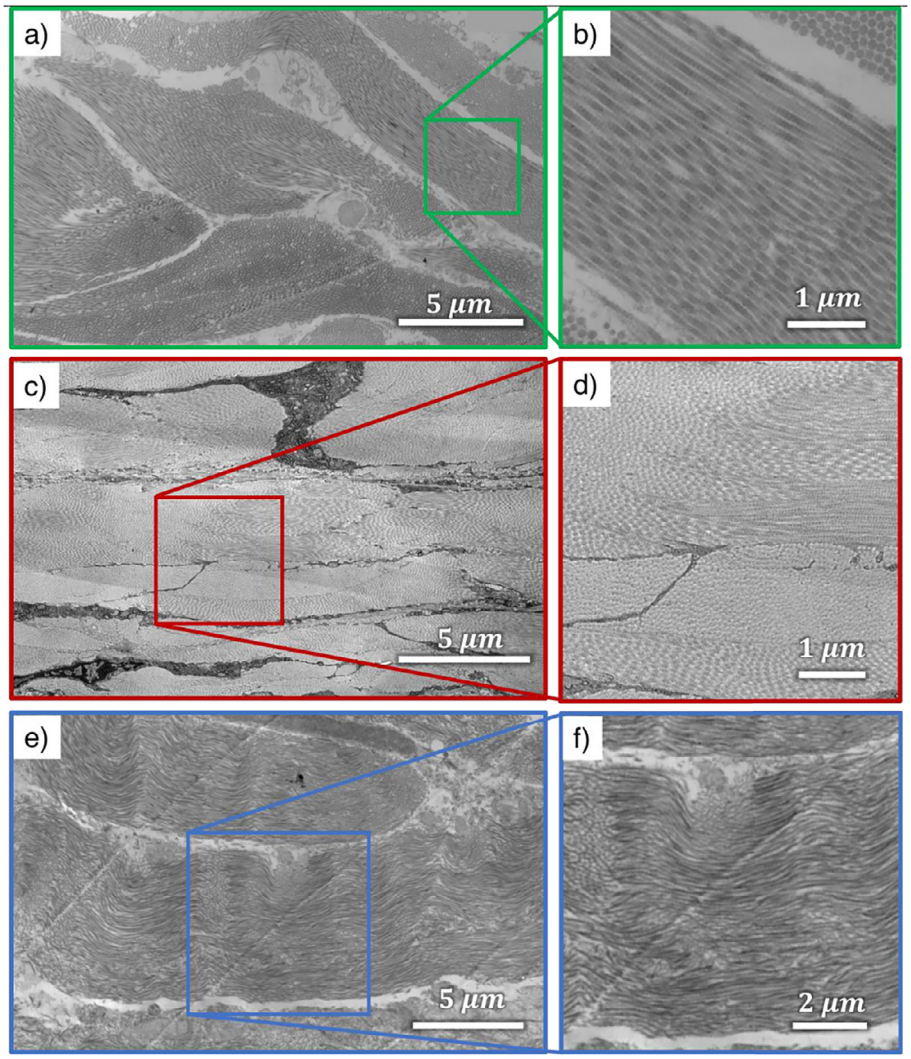

Fig. 12. Configuration of collagen in deformed (to failure) skin in three orientations; (a and b) longitudinal, (c and d) transverse, and (e and f) horizontal (parallel to the outer surface) sections, visualized by transmission electron microscopy. Collagen fibers were straightened during the deformation process, and appear to be more confined in the horizontal plane. In the transverse orientation, fibers mostly appear to going out of plane. Square inserts in (a, c and e) indicate the location of the magnified images in (b, d and f).

Observation on planes perpendicular to the dermis surface enable a look at this structure that has only been quantitatively characterized before by Nesbitt el al. [53]. Confocal microscopy conducted at three depth intervals of the cross section of the dermis is shown in Fig. 15a–c and Fig. 15f. It is clear that the collagen fibers are not arranged in layers parallel to the skin surface. Sherman et al. [11] observed a simpler arrangement for rabbit dermis and were able to peel layers parallel to the surface. Sections at 0 μm, 7.4 μm, and 13.3 μm show the waviness of the collagen with a radius of approximately 5 μm, as described in Fig. 14. The fibers are oriented at different angles but there seems to be two main perpendicular directions, as quantified earlier by Jor et al. [16]. The same configuration with higher magnification is shown in the SEM micrographs of Fig. 15d and e, where twisted braid-like structures can be discerned.

The tridimensional character of the fiber arrangement is clearly demonstrated. Indeed, this tridimensional arrangement can generate a mechanical response that is unique because the straightening of the fibers in tension is constrained by the neighboring bundles. This configuration is akin to the one in braided filamentary structures. In order to test the hypothesis of constitutive dependence of the mechanical response on the arrangement of fiber bundles, a simple model experiment was performed using hair bundles. Straight hair was organized into three bundles and braided into a tress (Fig. 16a). Each bundle had approximately 2000 hairs. The simplified schematic in Fig. 16b shows that, on top of the applied tensile load Fx_2, contact forces from neighboring hair bundles (or collagen fibers in the case of skin) oppose the straightening mechanism. We hypothesize that this can be approximated by a distributed force $Fx_1(X_2, \varepsilon)$ applied on the concave surface of the bundle and depending on the proximity to the neutral axis as well as the deformation state. The tensile response was determined and is shown in Fig. 16c, together for a single hair. The difference is dramatic and the J-curve behavior exhibited by the braid is strongly reminiscent of skin. This response of the braid is produced by the interaction among the hair bundles and not by their permanent

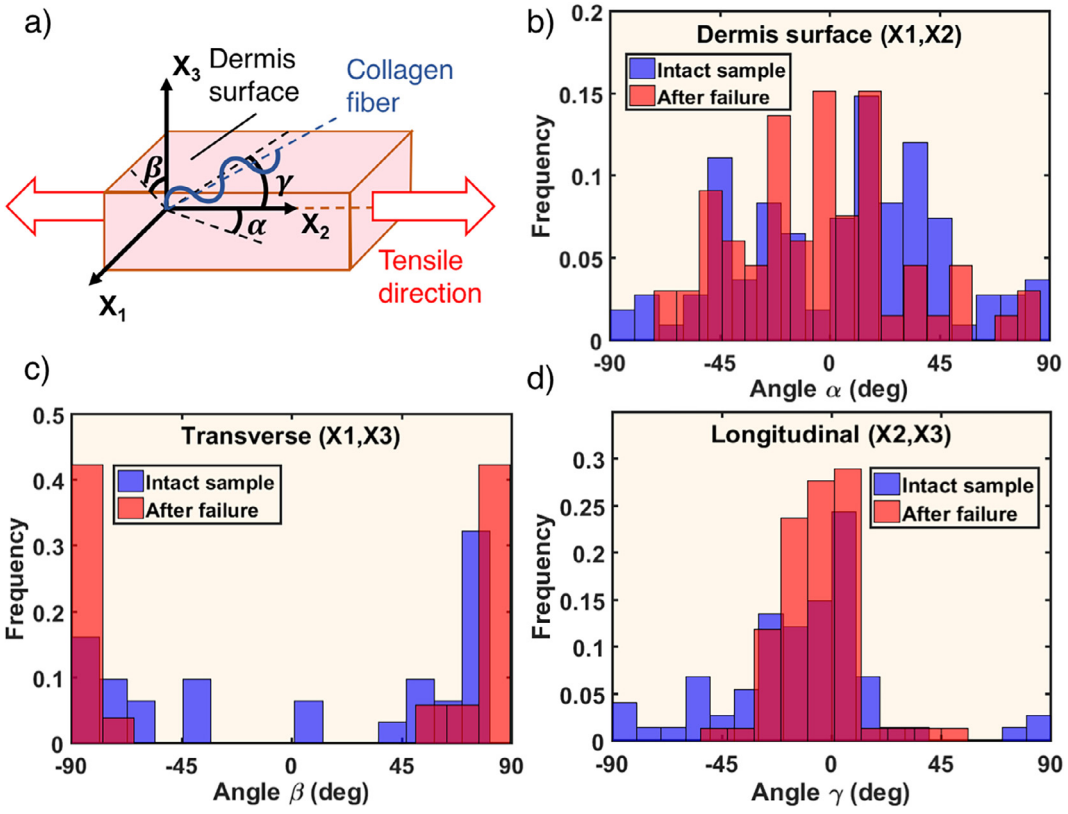

Fig. 13. Distribution of orientations of collagen fibers measured by angles (α, β, γ) of diametral lines with the tensile direction in intact samples and after failure. Planes of observation and corresponding angles are illustrated in (a), the tensile direction coinciding with the direction of the Langer lines. Note an increase in concentrations close to 0° with the tensile direction in the (b) horizontal and (d) longitudinal planes, and consequently a realignment close to ±90° in the (c) transverse direction in the failed sample.

deformation, which has its onset at 150 MPa for human hair [70]. The hysteresis exhibited upon unloading is also present, in a manner similar to skin. The onset of the linear regime occurs at a lower strain than for skin, but this is a parameter that can be manipulated by varying the tightness of the hair braiding. This model experiment demonstrates that the mechanical response of the dermis is influenced by the tridimensional organization of the collagen fibers.

4. Conclusions

The present study provides a complete experimental characterization of the uniaxial tensile behavior of skin, showing that it is a non-linear elastic material exhibiting sensitivity to time dependent and loading history dependent processes, i.e. strain rate, relaxation, and cyclic loading. Cross sample and intra-sample variations are both reported and quantified. An important finding is that viscoelastic processes are mainly determined by the level of applied stress, while a strain-based comparison results in very dispersed data due to large variations in terms of toe width and failure strain. Sample orientation has only little influence on the viscoelasticity of the tissue, although cyclic tests on transverse samples are missing and the determination of the dissipated energy would provide additional information.

The evolution of the Poisson ratio during deformation is presented here for the first time, to our knowledge. The different trends observed for transverse and longitudinal samples are of particular interest, and are indicators of different rearrangement processes occurring within the microstructure of the dermis. Other measurements indicate that this evolution, and particularly the initial offset of the Poisson ratio, is also dependent of the region of the body where the sample is taken. Loading/unloading tests show that this process is irreversible, with the Poisson ratio at unloading following a different path than during the loading cycle, similarly to the Mullins effect for the tangent modulus [8]. The particularly extreme values of the coefficient (from −1.2 to 0 for longitudinal samples and from 1 to 2.5 for transverse samples), as well as the global convergence towards values above 0.5 could be caused by a significant variation of local tissue anisotropy, and raise an interesting question regarding tissue incompressibility. Synchronous measurements in the lateral and in the thickness direction show that swelling occurs, and is initiated early in the deformation for some samples. Lees et al. [51] pointed out that comparable values can be observed for knitted fabrics, where the presence of voids affects the apparent volume of the material. Van Paepegem et al. [68] demonstrated that fiber reinforced composites can have negative Poisson ratios after repeated loading/unloading cycles, reflecting an increase of microstructural damages. We have shown that for skin, damage initiates very early in the deformation process. Note also that the measurement of the Poisson ratios used here is a linearized ratio of the strain in the transverse directions over the strain in the tensile direction, and thus directly depend on the reference configuration of the material. A factor of considerable importance in the method implemented in this study is that

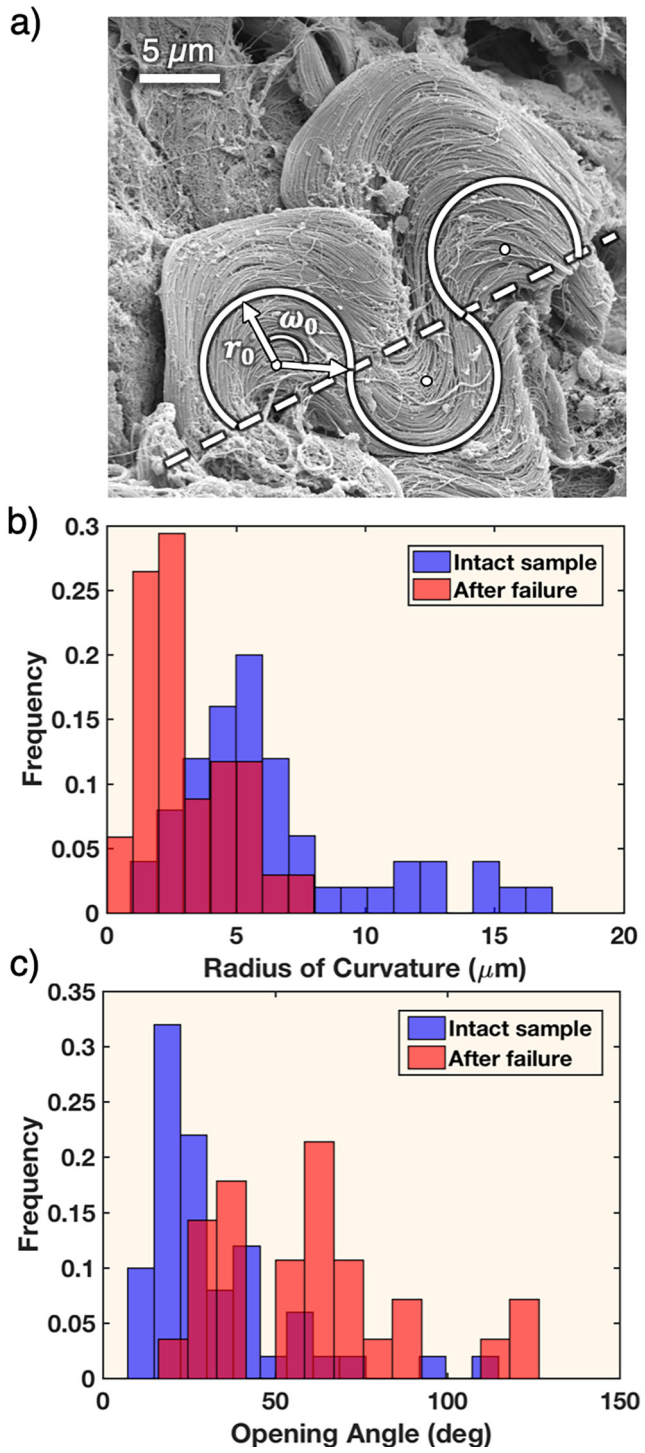

Fig. 14. Configuration and radii of curvature of collagen fibers in intact sample and after failure. (a) Scanning electron micrograph of a collagen fiber in the dermis of pig skin, superposed by a simplified representation of the wavy collagen fibers. Semi-circular segments with radius of curvature r_0 and opening angle ω_0 (in the initial configuration) describe the neutral axis of a fiber. Distribution of (b) radii of curvature r and (c) opening angle ω in intact (N = 50) and deformed (N = 33) collagen fibers.

skin samples are tested *ex vivo*, meaning that in they are not in their natural configuration when loaded on the uniaxial tensile setup. Post excision, samples can contract or expand in different ways based on their orientation and the region of the body they are taken from. It is therefore important to complement these results in the future to better identify the correlation between orientation and body region (for which the distribution of the collagen network vary), tissue contraction, and the evolution of the mechanical parameters with deformation.

To understand the macroscopic deformation, it is equally important to characterize the microscopic rearrangement processes occurring in the dermis. We provide quantitative data describing the straightening, but also the reorientation of collagen fibers before testing and after tensile failure, as well as their dimensions and properties. We observe that fibers converge towards the direction of applied tension, with initially a bimodal distribution of fiber orientation around the tensile axis in the surface plane changing to a narrower distribution with a single peak. This is similar to results reported by Yang et al. [19] by Small Angle X-Ray Scattering and *ex situ* Scanning Electron Microscopy, by Nesbitt et al. [53] by *in situ* Second Harmonic Generation Imaging, and earlier by Brown et al. [21] via *ex situ* Scanning Electron Microscopy, except that measurements are expanded to three dimensions in this work. Unexpectedly, we measure an increase of the curvature and of the opening angle of collagen, incompatible with fiber straightening, although qualitatively visualized by Transmission Electron Microscopy. We hypothesize that tissue failure causes the collagen fibers to recoil, with therefore smaller radii of curvature. *In situ* measurements or *ex situ* characterization at lower levels of strain can help expanding our understanding of the mechanism. Finally, the three-dimensional configuration of collagen fibers is evidenced in pig skin. Earlier descriptions of the dermis [11] mention a layered disposition of adjacent collagen fibers, parallel to the surface of the dermis, or a non-interacting collagenous network [6,25]. A consequence of this representation is that fiber-fiber interactions are clearly neglected, and most structurally-based constitutive models, such as the Gasser-Ogden-Holzapfel model [71], the Lanir model [25], or the Weiss model [72], ignore this contribution. The contribution of elastin to the mechanical response and the collagen network interconnectivity is not evidenced here. Imaging of the dermis in this work also shows an interwoven network of collagen fibers, with the presence of some twisted and braid-like structures. Our model experiment with a triple braided tress of hair demonstrates the influence of such a configuration on the mechanical response when compared to a single hair, with non-linear elasticity and energy dissipation. Resultantly, we suggest that future constitutive models should account for such deformation mechanisms for improved accuracy. Fundamental constituents in skin, such as hair follicles, nerve endings, and glands, are likely to be better protected during tensile deformation with the surrounding collagenous scaffold is not only restricted to one plane [53]. Differences in constituents, arrangement, or thickness also need to be taken into account when comparing results across species, for cases when results on animal skins need to be correlated with human skin, in applications of biomedical devices for example. Wei et al. [73] reported that skin thickness and elastic modulus scale allometrically with body size, while viscoelastic properties do not vary much between species. They conclude that rabbit and pig skin are suitable for pre-clinical testing, the as experimental results can be translated to humans by taking into account the identified scaling relationships. Differences in the arrangement of the collagenous network, and the corresponding dimensions, have not been reported, to our knowledge.

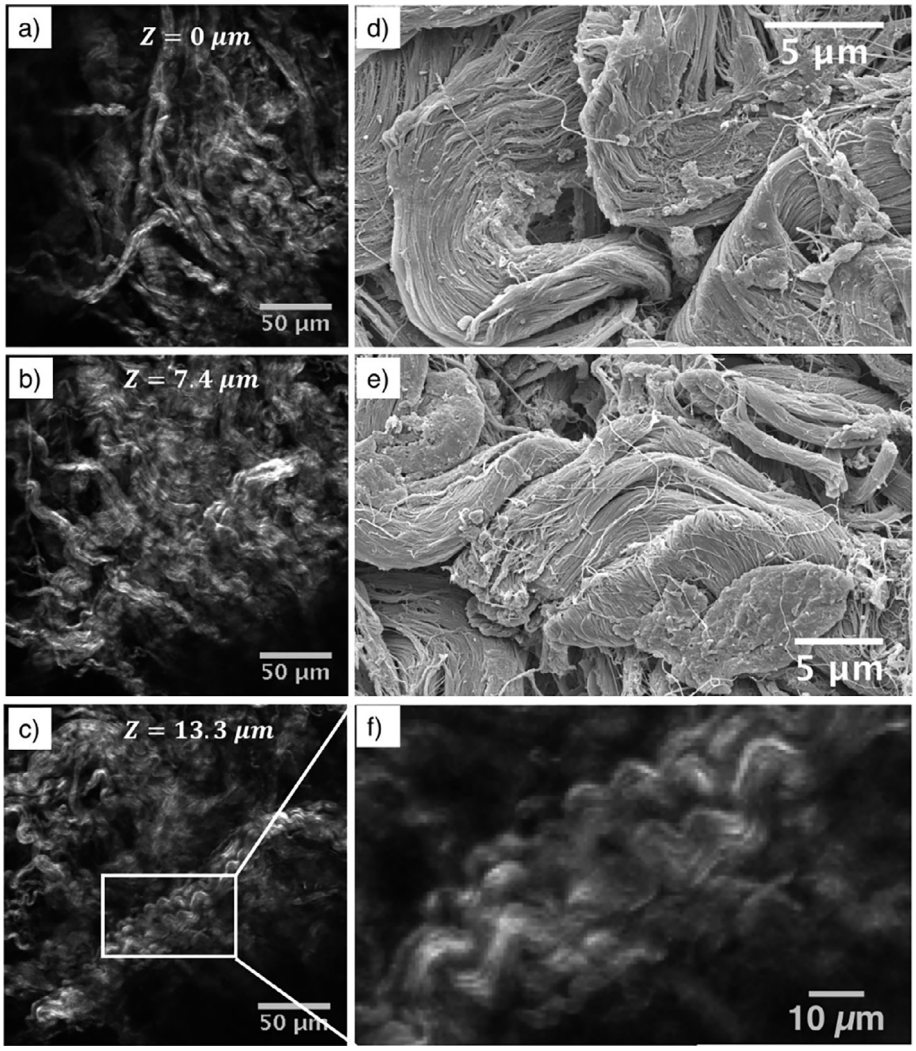

Fig. 15. Cross section views of pig skin dermis, showing the tridimensional arrangement of the collagen fiber network, and a certain degree of entanglement. (a–c) Confocal images with second harmonic generation fluorescence of collagen, captured at different intervals of depth. Oblique, wavy, perpendicular, fibers are superposed at different locations throughout the depth of the tissue, suggesting an interwoven pattern. (d and e) Scanning electron micrographs of collagen fibers, with folds and braid-like arrangements demonstrating the non-planar configuration. (f) Close up view of (c) showing collagen crimp and entanglement.

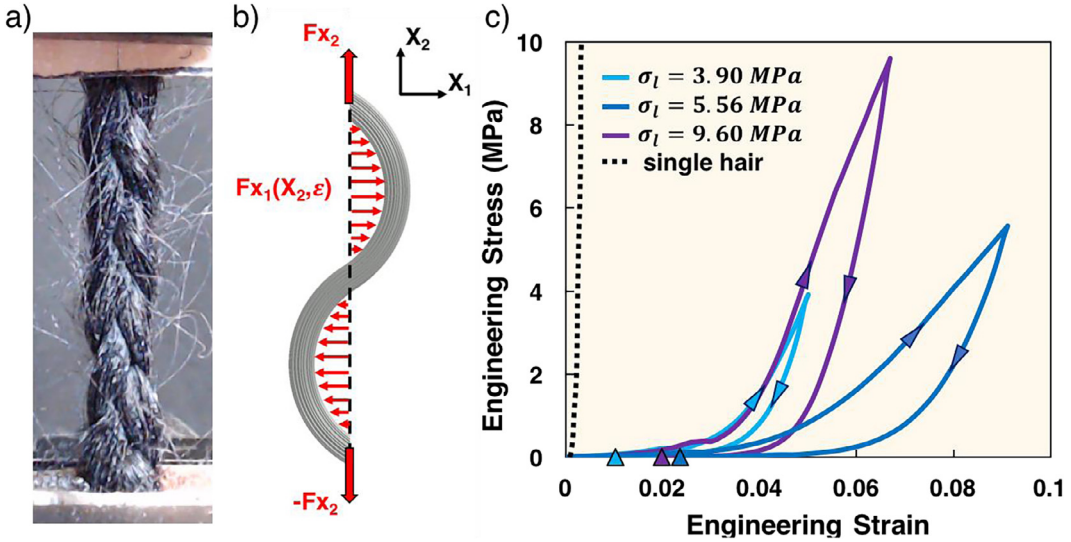

Fig. 16. (a) Mechanical test on a triple braid of hair, used as an analogy for the arrangement of some collagen fibers in the dermis. (b) Simplified two-dimensional representation of the forces acting on one bundle of hair/fibrils under a tensile load Fx_2. The neighboring bundles apply contact forces, modeled here as a distributed load Fx_1, which depends on the position X_2 and the deformation state ε. (c) Loading/unloading tests of different hair braids, with loading cycle stopped at different stresses. A hysteresis can be observed for each case, and remnant strains are present at unloading, indicated by arrows. Note also the J-shaped loading curve.

Acknowledgements

This work was partially funded by a Multi-University Research Initiative (grant no. AFOSR-FA9550-15-1-0009) from the Air Force Office of Scientific Research to the University of California Riverside, through subcontracts to the University of California, San Diego and the University of California, Berkeley. K.A.B and W.G.P. acknowledge the Royal British Legion for its support of the Centre for Blast Injury Studies at Imperial College London. W.G.P. also acknowledges support from AWE and Imperial College London. K.A.B. acknowledges additional support from the Isaac Newton Trust and the Global Alliance at the University of Cambridge, and the European Office of Aerospace Research and Development (grant no. AFOSR-FA9550-17-1-0214). The authors thank Dr. Dan Tucker from the Department of Veterinary Medicine, University of Cambridge, for sample provision, Dr. Benjamin Butler from the Department of Physics, Cavendish Laboratory, University of Cambridge for provision of resources and assistance during experiments, as well as Mr. Andrew Rayment from the Mechanical Testing Laboratory, Department of Materials Science & Metallurgy, University of Cambridge for instructions on tensile measurements. Their help was crucial to the successful conduct of this project. The authors greatly benefited from the advice given by Dr. Vincent Sherman and by and Dr. Aisling Ní Annaidh, whose respective experiences with working on skin led to important adaptations to the methods. We also acknowledge the use of the UCSD Cryo-Electron Microscopy Facility, supported by NIH grants to Dr. Timothy S. Baker and a gift from the Agouron Institute to UCSD. We finally thank Mason Mackey at the National Center for Microscopy and Imaging Research at UCSD, whose instructions on TEM sample preparation were indispensable.

Appendix A. Supplementary data

Supplementary data to this article can be found online at https://doi.org/10.1016/j.actbio.2019.01.023.

References

[1] B.J. Butler, R.L. Boddy, C. Bo, H. Arora, A. Williams, W.G. Proud, K.A. Brown, Composite nature of fresh skin revealed during compression, Bioinspired Biomimetic Nanobiomater. 4 (2015) 133–139, https://doi.org/10.1680/bbn.14.00028.
[2] J.T. Whitton, J.D. Everall, On the thickness of the epidermis, Br. J. Dermatol. 89 (1973).
[3] M. Huzaira, F. Rius, M. Rajadhyaksha, R.R. Anderson, S. González, Topographic variations in normal skin, as viewed by in vivo reflectance confocal microscopy, J. Invest. Dermatol. 116 (2001) 846–852, https://doi.org/10.1046/j.0022-202X.2001.01337.x.
[4] J.W.Y. Jor, M.D. Parker, A.J. Taberner, M.P. Nash, P.M.F. Nielsen, Computational and experimental characterization of skin mechanics: identifying current challenges and future directions, Wiley Interdiscip. Rev. Syst. Biol. Med. 5 (2013) 539–556, https://doi.org/10.1002/wsbm.1228.
[5] G.L. Wilkes, I.A. Brown, R.H. Wildnauer, The biomechanical properties of skin, CRC Crit. Rev. Bioeng. 1 (1973) 453–495. http://www.ncbi.nlm.nih.gov/pubmed/4581809.
[6] G. Limbert, Mathematical and computational modelling of skin biophysics: a review, Proc. R. Soc. A Math. Phys. Eng. Sci. 473 (2017).
[7] G.G. Barbarino, M. Jabareen, E. Mazza, Experimental and numerical study on the mechanical behavior of the superficial layers of the face, Ski. Res. Technol. 17 (2011) 434–444, https://doi.org/10.1111/j.1600-0846.2011.00515.x.
[8] M.J. Muñoz, J.A. Bea, J.F. Rodríguez, I. Ochoa, J. Grasa, A. Pérez del Palomar, P. Zaragoza, R. Osta, M. Doblaré, An experimental study of the mouse skin behaviour: Damage and inelastic aspects, J. Biomech. 41 (2008) 93–99, https://doi.org/10.1016/j.jbiomech.2007.07.013.
[9] Y. Lanir, Y.C. Fung, Two-dimensional mechanical properties of rabbit skin—II. experimental results, J. Biomech. 7 (1974) 171–182, https://doi.org/10.1016/0021-9290(74)90058-X.
[10] V.R. Sherman, W. Yang, M.A. Meyers, The materials science of collagen, J. Mech. Behav. Biomed. Mater. 52 (2015) 22–50, https://doi.org/10.1016/j.jmbbm.2015.05.023.
[11] V.R. Sherman, Y. Tang, S. Zhao, W. Yang, M.A. Meyers, Structural characterization and viscoelastic constitutive modeling of skin, Acta Biomater. (2017), https://doi.org/10.1016/j.actbio.2017.02.011.
[12] M.A. Meyers, P.-Y. Chen, Biological Materials Science, Cambridge University Press, 2014.
[13] K. Langer, On the anatomy and physiology of the skin, Br. J. Plast. Surg. 31 (1978) 3–8, https://doi.org/10.1016/0007-1226(78)90003-6.
[14] H.T. Cox, The cleavage lines of the skin, Br. J. Surg. 29 (1941) 234–240, https://doi.org/10.1002/bjs.18002911408.
[15] M. Kwak, D. Son, J. Kim, K. Han, Static Langer's line and wound contraction rates according to anatomical regions in a porcine model, Wound Repair Regener. 22 (2014) 678–682, https://doi.org/10.1111/wrr.12206.
[16] J.W.Y. Jor, P.M.F. Nielsen, M.P. Nash, P.J. Hunter, Modelling collagen fibre orientation in porcine skin based upon confocal laser scanning microscopy, Skin Res. Technol. (2011) 149–159, https://doi.org/10.1111/j.1600-0846.2010.00471.x.
[17] O. Lokshin, Viscoelasticity and preconditioning of rat skin under uniaxial stretch: microstructural constitutive characterization, J. Biomech. Eng. 131 (2009) 31009, https://doi.org/10.1115/1.3049479.
[18] A.D. Freed, T.C. Doehring, Elastic model for crimped collagen fibrils, J. Biomech. Eng. 127 (2005) 587–593, https://doi.org/10.1115/1.1934145.
[19] W. Yang, V.R. Sherman, B. Gludovatz, E. Schaible, P. Stewart, R.O. Ritchie, M.A. Meyers, On the tear resistance of skin, Nat. Commun. 6 (2015) 6649, https://doi.org/10.1038/ncomms7649.
[20] J.W.Y. Jor, M.P. Nash, P.M.F. Nielsen, P.J. Hunter, Estimating material parameters of a structurally based constitutive relation for skin mechanics, Biomech. Model. Mechanobiol. 10 (2011) 767–778, https://doi.org/10.1007/s10237-010-0272-0.
[21] I.A. Brown, A scanning electron microscope study of the effects of uniaxial tension on human skin, Br. J. Dermatol. 89 (1973) 383–393, https://doi.org/10.1111/j.1365-2133.1973.tb02993.x.
[22] S.M. Belkoff, R.C. Haut, A structural model used to evaluate the changing microstructure of maturing rat skin, J. Biomech. 24 (1991) 711–720, https://doi.org/10.1016/0021-9290(91)90335-K.
[23] G.D. Weinstein, R.J. Boucek, Collagen and elastin of human dermis, J. Invest. Dermatol. 35 (1960) 227–229. http://www.ncbi.nlm.nih.gov/pubmed/13783962.
[24] A.J. Gallagher, A. Ni Anniadh, K. Kruyere, M. Ottenio, H. Xie, M.D. Gilchrist, Dynamic tensile properties of human skin, 2012 IRCOBI Conf. (2012) 494–502. doi:Irc-12-59.
[25] Y. Lanir, A structural theory for the homogeneous biaxial stress-strain relationships in flat collagenous tissues, J. Biomech. 12 (1979) 423–436, https://doi.org/10.1016/0021-9290(79)90027-7.
[26] H. Oxlund, J. Manschot, A. Viidik, The role of elastin in the mechanical properties of skin, J. Biomech. 21 (1988) 213–218, https://doi.org/10.1016/0021-9290(88)90172-8.
[27] C. Escoffier, J. de Rigal, A. Rochefort, R. Vasselet, J.-L. Leveque, P.G. Agache, Age-related mechanical properties of human skin: an in vivo study, J. Invest. Dermatol. 93 (1989) 353–357, https://doi.org/10.1111/1523-1747.ep12280259.
[28] R. Sanders, Torsional elasticity of human skin in vivo, Pflugers Arch. Eur. J. Physiol. 342 (1973) 255–260, https://doi.org/10.1007/BF00591373.
[29] B. Finlay, Dynamic mechanical testing of human skin "in vivo", J. Biomech. 3 (1970), https://doi.org/10.1016/0021-9290(70)90040-0.
[30] B. Finlay, The torsional characteristics of human skin in vivo, Biomed. Eng. (NY) 6 (1971) 567–573. http://www.ncbi.nlm.nih.gov/pubmed/5158520.
[31] J.C. Dick, The tension and resistance to stretching of human skin and other membranes, with results from a series of normal and oedematous cases, J. Physiol. 112 (1951) 102–113. http://www.ncbi.nlm.nih.gov/pubmed/14825184.
[32] R. Grahame, P.J. Holt, The influence of ageing on the in vivo elasticity of human skin, Gerontologia 15 (1969) 121–139. http://www.ncbi.nlm.nih.gov/pubmed/5772167.
[33] T.K. Tonge, L.S. Atlan, L.M. Voo, T.D. Nguyen, Full-field bulge test for planar anisotropic tissues: part I-experimental methods applied to human skin tissue, Acta Biomater. 9 (2013) 5913–5925, https://doi.org/10.1016/j.actbio.2012.11.035.
[34] G.E. Piérard, S. Piérard, P. Delvenne, C. Piérard-franchimont, In Vivo Evaluation of the Skin Tensile Strength by the Suction Method : Pilot Study Coping with Hysteresis and Creep Extension, 2013 (2013).
[35] L. Pedersen, B. Hansen, G.B.E. Jemec, Mechanical properties of the skin: a comparison between two suction cup methods, Skin Res. Technol. 9 (2003) 111–115, https://doi.org/10.1034/j.1600-0846.2003.00021.x.
[36] C. Pailler-Mattei, S. Bec, H. Zahouani, In vivo measurements of the elastic mechanical properties of human skin by indentation tests, Med. Eng. Phys. 30 (2008) 599–606, https://doi.org/10.1016/j.medengphy.2007.06.011.
[37] C. Flynn, A. Taberner, P. Nielsen, Measurement of the force-displacement response of in vivo human skin under a rich set of deformations, Med. Eng. Phys. 33 (2011) 610–619, https://doi.org/10.1016/j.medengphy.2010.12.017.
[38] C. Flynn, A. Taberner, P. Nielsen, Mechanical characterisation of in vivo human skin using a 3D force-sensitive micro-robot and finite element analysis, Biomech. Model. Mechanobiol. 10 (2011) 27–38, https://doi.org/10.1007/s10237-010-0216-8.
[39] G. Boyer, L. Laquièze, A. Le Bot, S. Laquièze, H. Zahouani, Dynamic indentation on human skin in vivo: Ageing effects, Skin Res. Technol. 15 (2009) 55–67, https://doi.org/10.1111/j.1600-0846.2008.00324.x.

[40] A. Ní Annaidh, K. Bruyère, M. Destrade, M.D. Gilchrist, M. Otténio, Characterization of the anisotropic mechanical properties of excised human skin, J. Mech. Behav. Biomed. Mater. 5 (2012) 139–148, https://doi.org/10.1016/j.jmbbm.2011.08.016.
[41] M. Ottenio, D. Tran, A. Ní Annaidh, M.D. Gilchrist, K. Bruyère, Strain rate and anisotropy effects on the tensile failure characteristics of human skin, J. Mech. Behav. Biomed. Mater. 41 (2015) 241–250, https://doi.org/10.1016/j.jmbbm.2014.10.006.
[42] A.E. Ehret, M. Hollenstein, E. Mazza, M. Itskov, Porcine dermis in uniaxial cyclic loading: Sample preparation, experimental results and modeling, J. Mech. Mater. Struct. 6 (2011) 1125–1135, https://doi.org/10.2140/jomms.2011.6.1125.
[43] K.H. Lim, C.M. Chew, P.C.Y. Chen, S. Jeyapalina, H.N. Ho, J.K. Rappel, B.H. Lim, New extensometer to measure in vivo uniaxial mechanical properties of human skin, J. Biomech. 41 (2008) 931–936, https://doi.org/10.1016/j.jbiomech.2008.01.004.
[44] B. Zhou, F. Xu, C. Chen, T. Lu, Strain rate sensitivity of skin tissue under thermomechanical loading, Philos. Trans. R. Soc. A Math. Phys. Eng. Sci. 368 (2010) 679–690, https://doi.org/10.1098/rsta.2009.0238.
[45] J. Ankersen, A.E. Birkbeck, R.D. Thomson, P. Vanezis, Puncture resistance and tensile strength of skin simulants, Proc. Inst. Mech. Eng. H. 213 (1999) 493–501, https://doi.org/10.1243/0954411991535103.
[46] Y. Lanir, Y.C. Fung, Two-dimensional mechanical properties of rabbit skin—I. experimental system, J. Biomech. 7 (1974) 29–34, https://doi.org/10.1016/0021-9290(74)90067-0.
[47] D.C. Schneider, T.M. Davidson, In vitro biaxial stress-strain response of human skin, Arch Otolaryngol. 110 (1984) 329–333. http://www.ncbi.nlm.nih.gov/pubmed/6712522.
[48] Y.A. Kvistedal, P.M.F. Nielsen, Estimating material parameters of human skin in vivo, Biomech. Model. Mechanobiol. 8 (2009) 1–8, https://doi.org/10.1007/s10237-007-0112-z.
[49] X. Liang, S.A. Boppart, Biomechanical properties of in vivo human skin from dynamic optical coherence elastography, IEEE Trans. Biomed. Eng. 57 (2010) 953–959, https://doi.org/10.1109/TBME.2009.2033464.
[50] F.M. Hendriks, D. Brokken, C.W.J. Oomens, D.L. Bader, F.P.T. Baaijens, The relative contributions of different skin layers to the mechanical behavior of human skin in vivo using suction experiments, Med. Eng. Phys. 28 (2006) 259–266, https://doi.org/10.1016/j.medengphy.2005.07.001.
[51] C. Lees, J.F. Vincent, J.E. Hillerton, Poisson's ratio in skin, Biomed. Mater. Eng. 1 (1991) 19–23. http://www.ncbi.nlm.nih.gov/pubmed/1842507.
[52] M.S. Sacks, Incorporation of experimentally-derived fiber orientation into a structural constitutive model for planar collagenous tissues, J. Biomech. Eng. 125 (2003) 280–287, https://doi.org/10.1115/1.1544508.
[53] S. Nesbitt, W. Scott, J. Macione, S. Kotha, Collagen fibrils in skin orient in the direction of applied uniaxial load in proportion to stress while exhibiting differential strains around hair follicles, Materials (Basel) 8 (2015) 1841–1857, https://doi.org/10.3390/ma8041841.
[54] Standard Test Methods for Vulcanized Rubber and Thermoplastic Elastomers—Tension, (n.d.). <https://www.astm.org/Standards/D412.htm>.
[55] J. Blaber, B. Adair, A. Antoniou, Ncorr: open-source 2D Digital Image Correlation Matlab Software, Exp. Mech. 55 (2015) 1105–1122, https://doi.org/10.1007/s11340-015-0009-1.
[56] R.H. Pritchard, P. Lava, D. Debruyne, E.M. Terentjev, Precise determination of the Poisson ratio in soft materials with 2D digital image correlation, Soft Matter 9 (2013) 6037–6045, https://doi.org/10.1039/c3sm50901j.
[57] X. Chen, O. Nadiarynkh, S. Plotnikov, P.J. Campagnola, Second harmonic generation microscopy for quantitative analysis of collagen fibrillar structure, Nat. Protoc. 7 (2012) 654–669, https://doi.org/10.1038/nprot.2012.009.
[58] F. Maceri, M. Marino, G. Vairo, A unified multiscale mechanical model for soft collagenous tissues with regular fiber arrangement, J. Biomech. 43 (2010) 355–363, https://doi.org/10.1016/j.jbiomech.2009.07.040.
[59] Y.C. Fung, Elasticity of soft tissues in simple elongation, Am. J. Physiol. 213 (1967) 1532–1544.
[60] Y. Lanir, Structure-strength relations in mammalian tendon, Biophys. J. 24 (1978) 541–554, https://doi.org/10.1016/S0006-3495(78)85400-9.
[61] M.G. Dunn, F.H. Silver, Viscoelastic behavior of human connective tissues: relative contribution of viscous and elastic components, Connect. Tissue Res. 12 (1983) 59–70, https://doi.org/10.3109/03008208309005612.
[62] M.A. Meyers, Dynamic Behavior of Materials, John Wiley & Sons, Inc., Hoboken, NJ, USA, 1994. doi:10.1002/9780470172278.
[63] G.A. Holzapfel, R.W. Ogden, On planar biaxial tests for anisotropic nonlinearly elastic solids. a continuum mechanical framework, Math. Mech. Solids. 14 (2009) 474–489, https://doi.org/10.1177/1081286507084411.
[64] O. Emile, A. Le Floch, F. Vollrath, Time-resolved torsional relaxation of spider draglines by an optical technique, Phys. Rev. Lett. 98 (2007), https://doi.org/10.1103/PhysRevLett. 98.167402.
[65] Y. Yu, W. Yang, M.A. Meyers, Viscoelastic properties of α-keratin fibers in hair, Acta Biomater. 64 (2017) 15–28, https://doi.org/10.1016/j.actbio.2017.09.012.
[66] C.P. Waddington, Viscoelastic parameter determination from cyclic loading tests: application to adhesive flow in the microtensile testing of whisker crystals, J. Phys. D Appl. Phys. 5 (1972) 1531–1539, https://doi.org/10.1088/0022-3727/5/9/307.
[67] A.S. Caro-Bretelle, P. Ienny, R. Leger, S. Corn, I. Bazin, F. Bretelle, Constitutive modeling of stress softening and permanent set in a porcine skin tissue: impact of the storage preservation, J. Biomech. 49 (2016) 2863–2869, https://doi.org/10.1016/j.jbiomech.2016.06.026.
[68] W. Van Paepegem, I. De Baere, E. Lamkanfi, J. Degrieck, Monitoring quasi-static and cyclic fatigue damage in fibre-reinforced plastics by Poisson ' s ratio evolution, Int. J. Fatigue 32 (2010) 184–196, https://doi.org/10.1016/j.ijfatigue.2009.02.026.
[69] N.J. Vardaxis, T.A. Brans, M.E. Boon, R.W. Kreis, L.M. Marres, Confocal laser scanning microscopy of porcine skin: implications for human wound healing studies, J. Anat. 190 (1997) 601–611, https://doi.org/10.1046/j.1469-7580.1997.19040601.x.
[70] Y. Yu, W. Yang, B. Wang, M.A. Meyers, Structure and mechanical behavior of human hair, Mater. Sci. Eng. C. 73 (2017) 152–163, https://doi.org/10.1016/j.msec.2016.12.008.
[71] T.C. Gasser, R.W. Ogden, G.A. Holzapfel, Hyperelastic modelling of arterial layers with distributed collagen fibre orientations, J. R. Soc. Interface 3 (2006) 15–35, https://doi.org/10.1098/rsif.2005.0073.
[72] R.B. Groves, S.A. Coulman, J.C. Birchall, S.L. Evans, An anisotropic, hyperelastic model for skin: Experimental measurements, finite element modelling and identification of parameters for human and murine skin, J. Mech. Behav. Biomed. Mater. 18 (2013) 167–180, https://doi.org/10.1016/j.jmbbm.2012.10.021.
[73] J.C.J. Wei, G.A. Edwards, D.J. Martin, H. Huang, M.L. Crichton, M.A.F. Kendall, Allometric scaling of skin thickness, elasticity, viscoelasticity to mass for micro-medical device translation: from mice, rats, rabbits, pigs to humans, Sci. Rep. 7 (2017) 1–17, https://doi.org/10.1038/s41598-017-15830-7.